INTERNATIONAL JOURNAL FOR NUMERICAL METHODS IN FLUIDS, VOL. 26, 251–280 (1998)

A STABLE ALGORITHM FOR REYNOLDS STRESS TURBULENCE MODELLING WITH APPLICATIONS TO RECTILINEAR AND CIRCULAR TIDAL FLOWS

S. G. SAJJADI* AND M. N. WAYWELL

Centre for Computational Fluid Dynamics and Turbulence, University of Salford, Salford M5 4WT, U.K.

SUMMARY

This paper employs one-point, linear eddy viscosity and differential second-moment (DSM) turbulence closures to predict the turbulent characteristics of both rectilinear and circular tidal flows. The numerical scheme is based on a finite volume approach applied to a non-staggered grid such that all flow variables are stored at one and the same set of nodes. Numerical stability is maintained through the implementation of apparent viscosities and source term linearization, which are essential if eddy viscosity terms are absent. A stable algorithm is devised for the Reynolds stresses which includes a non-linear velocity smoothing in order to stabilise the numerical scheme during flow reversal and relaminarization. Favourable agreement with the experimental rectilinear tidal data of Schröder (*Tech. Rep. GK55 87/E/16*, GKSS-Forshungszentrum Geesthacht, 1983) and McClean (*Turbulence and Sediment Transport Measurements in a North Sea Tidal Inlet (the Jade)*, Springer, New York, 1987, p. 436) is reported. Numerical calculations of circular tidal flows are also presented which were motivated by the preliminary investigations of Davies and Jones (*Int. j. numer. meth. fluids*, **12**, 17 (1991)) and Davies (*Continental Shelf. Res.*, **11**, 1313 (1991)), who employed the one-equation, $k-l$, eddy viscosity turbulence model to simulate rectilinear and circular tidal flows. © 1998 John Wiley & Sons, Ltd.

Int. J. Numer. Meth. Fluids, **26**: 251–280 (1998).

KEY WORDS: turbulence modelling; eddy viscosity; second-moment closure; tidal flows; finite volume

1. INTRODUCTION

A major source of turbulence produced in the near-bed region of shallow homogeneous seas is due to fluid motions over rough sea beds. This turbulence is primarily generated by currents associated with wind-, tide- and wave-induced motions.[1,2] The enhanced physical effects of the generated turbulence include faster mixing and momentum rates, increased bed stress and higher levels of energy. In general these factors cannot be ignored by coastal engineers who are interested in predictions of sediment transport, pollutant redistribution, bed erosion and coastal defence.

In large-scale three-dimensional hydrodynamic models of tidal flow[3] a slip bottom boundary condition is applied at a height 100 cm above the bed where the bed stress is related to the slip

---

*Correspondence to: S. G. Sajjadi, Centre for Computational Fluid Dynamics and Turbulence, University of Salford, Salford M5 4WT, U.K.

CCC 0271–2091/98/030251–30 $17.50

Received November 1995
Revised March 1997

velocity U_b at the bottom boundary by $\tau = \rho C_{100} U_b^2$, where ρ is the density of the fluid and C_{100} is the drag coefficient evaluated at 100 cm above the bed. This drag coefficient is a function of the bed roughness and is affected by the presence of small-scale bed features. These small-scale features cannot be resolved by large-scale models which might cover areas extending over many hundreds of kilometres. Hence the effect of these small-scale features can only be parametrized in large-scale models. The appropriate value of C_{100} can in principle be determined through detailed modelling of the near-bed turbulence.

To date, numerical investigations of both rectilinear and circular tidal flows have been limited to the simplest linear eddy viscosity turbulence models. Davies and Jones[1] applied the one-equation $k-l$ model to investigate the effects of wind and tidal flows on the turbulent boundary layer. Furthermore, Davies[4] examined the influence of eddy viscosity in both rectilinear and circular tidal flows. Baumert and Radach[5] applied the two-equation $k-\varepsilon$ model to rectilinear tidal flows and found that the results compared favourably with the experimental data of Schröder[6] and McClean.[7] However, it is well known that isotropic eddy viscosity models fail to resolve individual Reynolds stresses and do not capture the anisotropic Reynolds stress distribution in the vicinity of the bed. For example, the simulations of Sajjadi and Aldridge[8] of a steady flow traversing a stationary sand ripple demonstrate quite clearly that linear eddy viscosity models have difficulty in resolving the effects of streamwise curvature, which can either suppress or augment the relative levels of the Reynolds stresses. Since curved asymmetrical bed forms are frequently observed in near-shore shallow water regions and the effect of the Coriolis parameter is very influential in coastal engineering simulations, it may be tentatively suggested that when the effect of the Coriolis force is important, such as in the case of circular tides considered here, then linear eddy viscosity models may be inadequate to resolve the complex turbulent properties (such as the individual components of Reynolds stresses, since the Coriolis parameter enters into their transport equations) of ocean dynamics accurately.

A large proportion of such calculations hitherto have utilized a form of eddy viscosity model to represent the turbulent transport. In these approaches the Reynolds stresses are linearly related to the mean rate of strain via an eddy viscosity, and while this is often capable of providing reasonable results, it does have serious limitations. For instance, in the case of circular tides it is incapable of reproducing the effects due to the Coriolis force, which acts to either augment or suppress individual components of Reynolds stresses and cannot easily be embodied in an eddy viscosity formulation. Thus, to incorporate the effect due to rotation accurately, a more detailed description of the turbulent transport is required, such as the full differential second-moment closure (DSM) adopted here. Although eddy-viscosity-type models have proven to work well in shear-stress-dominated wall-bounded flows of engineering interest, there are many examples of situations in which they produce predictions that are far from the experimental results. One example is the case of rotating channel flow which was studied in detail by Launder *et al.*[9] The principal conclusion was that eddy viscosity two-equation models predict a symmetrical profile as in the case of non-rotating flow. This study displayed the inability of such models to handle the effects of rotation, on the individual components of Reynolds stresses, in an adequate way. Models based on the transport equations of the Reynolds stress tensor (DSM) closures have prerequisites for a better accommodation of the underlying physics of such flows. For a review on the subject the reader is referred to Reference 10. In the present paper we will consider DSM closure schemes for the transport of Reynolds stresses $\overline{u_i u_j}$ and the total dissipation rate ε.

The traditional prescription of boundary conditions for tidal flows (and rough oscillatory boundary layers in general) has been based on the key assumption that in the near-bed region the flow is always fully rough with fully developed turbulence. Therefore the transport equations are integrated directly down to the no-slip boundary condition, since it is assumed the effect of viscosity are generally small. Nevertheless, the preliminary calculations of Sajjadi and Waywell[11] (who investigated oscillatory flows driven by wind waves of period $t \approx 10\,\mathrm{s}$) indicate that in the context of oscillatory boundary layer flows this assumption may not always be valid over the entire phase cycle (particularly during the early stages of flow acceleration and around flow reversal). However, this work demonstrated that wind-induced and tidally induced ($T \approx 12\,\mathrm{h}$) flows share many common features, including

(i) hysteresis effects of turbulent energy due to the turbulence-bursting phenomenon which occurs shortly after pressure gradient reversal[12,13]
(ii) the existence of a logarithmic region above the bed similar to that observed in steady channel flow.[12]

Important differences between these types of flow are also evident, the main features being as follows:

(i) The maintenance of fully developed turbulence across the majority of the flow cycle is often observed in tidal problems. For example, Hamilton *et al.*[14] estimate that the Celtic Sea remains fully turbulent across 85% of the flow cycle.
(ii) Turbulent energy generated in the near-bed region in tidal flows is often diffused further away from the bed than in wind-wave-induced flows. This usually means that the observed turbulent boundary layer is not fully developed when it reaches the free surface, particularly in shallow water areas.

In the present paper we discard the traditional approach to boundary conditions in favour of slip boundary conditions, based on roughness-dependent wall functions,[8] which explicitly take into account the nature of the bed (be it hydraulically smooth, transitional or fully rough). In Section 6 we will make repeated reference to the 'near-wall' region. This of course refers to the near-bed flow region strictly *above* the semiviscous region where the high-Reynolds-number turbulence closures are no longer valid.

The numerical integration of the transport equations is based on a fully conservative, collocated finite volume scheme. However, the implementation of second-moment closure models with such a scheme leads to numerical instability owing to decoupling of the mean velocity and Reynolds stresses. This problem is overcome by adopting the concepts of apparent viscosity[15] and source term linearization.[16] However, one might ask, in particular with reference to the rectilinear tide, why one should adopt such a complicated scheme for a relatively simple problem. To answer this question, we should note that oscillatory flows, with or without rotation, are potentially unstable. The reason is that in these flows, through the action of shear layer instability, turbulence is generated in the near-wall region during the early phases of flow acceleration and is continuously diffused away towards the freestream region. However, a favourable pressure gradient suppresses the creation of turbulence. Following pressure gradient reversal, turbulence begins to grow violently and explosively at the bed and is sustained by turbulence bursting. As the pressure gradient becomes increasingly adverse, however, the flow relaminarizes. Aldridge[17] adopted a simple finite difference scheme for oscillatory flows and found that the scheme becomes very unstable during the stages of flow reversal, particularly when the flow relaminarizes. This has certainly been our experience too. Thus, to circumvent this difficulty, we have adopted the scheme originally developed by Lien and Leschziner[15] and included a non-linear velocity smoothing (see Section 4) in order to stabilise the scheme during flow reversal and when the flow relaminarizes.

Another interesting problem in an oscillatory flow is the question of transition. Does transition to turbulence occur in the first acceleration stage of oscillatory boundary layer flows? If so, what are the effects of the turbulence generated at the bed? Both these important questions must be addressed by coastal engineers who need to consider the extra stresses and momentum generated by turbulence that contribute to sea bed and coastal erosion, sediment transport and pollution redistribution. Although information on the laminar–turbulent transition process for oscillating boundary layer flows over both smooth and rough surfaces has been obtained experimentally, it is perhaps surprising that the mathematical modelling of the transition process is still quite poor. Numerical investigations of turbulent oscillatory boundary layers have recently received much attention; amongst others the recent work of Waywell and Sajjadi[18] is worth noting. Although good agreement with experimental data has been reported by these authors, e.g. capturing the general features of oscillatory flow, the subtle details of transition, particularly in the transitional phases, have so far proved to be a challenging task from the traditional one-point closure point of view.

2. MODEL EQUATIONS

The linearized, hydrodynamic boundary layer equations can be expressed as[19]

$$\rho\frac{\partial U}{\partial t}-2\rho\Omega W=\frac{\partial P}{\partial x}+\frac{\partial}{\partial y}\left(\mu\frac{\partial U}{\partial y}-\rho\overline{uv}\right),\qquad \rho\frac{\partial W}{\partial t}+2\rho\Omega U=-\frac{\partial P}{\partial z}+\frac{\partial}{\partial y}\left(\mu\frac{\partial W}{\partial y}-\rho\overline{vw}\right),\tag{1}$$

where y represents the vertical co-ordinate and the mean velocities U and W denote the Cartesian x- and z-components of the current respectively. The kinematic fluid viscosity $\nu = 1{\cdot}0\times10^{-6}\,\mathrm{m}^2\,\mathrm{s}^{-1}$ and the Coriolis parameter $\Omega = 6\times10^{-5}\,\mathrm{s}^{-1}$ are both assumed to be constant. At the edge of the boundary layer the mean velocity profiles at time t vary sinusoidally as

$$U=U_\infty\sin(\omega t),\qquad W=W_\infty\sin(\omega t),\tag{2}$$

where U_∞ and W_∞ represent the mean freestream velocities and $\omega = 2\pi/T$ is the frequency, T being the tidal period of oscillatory motion which is of the order of 12 h. In the freestream region the pressure gradient approximately balances the temporal velocity acceleration such that

$$\frac{\partial P}{\partial x}=-U_\infty\rho\omega\cos(\omega t-\phi_x),\qquad \frac{\partial P}{\partial z}=-W_\infty\rho\omega\cos(\omega t-\phi_z).\tag{3}$$

From equations (3) we define $\Phi = \phi_x - \phi_z$, which denotes the phase difference between the x- and z-forcing motions. If the boundary layer height is small compared with the vertical length scale, then it can be assumed that equations (3) are also valid in the boundary layer.

In order to solve equations (1), the Reynolds stresses $\overline{uv}$ and $\overline{vw}$ must be determined *a priori*. In the present investigation two closure schemes are adopted. The first is based on the eddy viscosity concept in which the Reynolds stresses are related to mean rates of strain such that

$$\overline{uv}=-\nu_\mathrm{t}\frac{\partial U}{\partial y},\qquad \overline{vw}=-\nu_\mathrm{t}\frac{\partial W}{\partial y},\tag{4}$$

where ν_t is the eddy viscosity given by the relationship[8]

$$\nu_\mathrm{t}=c_\mu k^2/\varepsilon\tag{5}$$

and $c_\mu = 0{\cdot}09$. The turbulent kinetic energy k is calculated from the transport equation[8]

$$\frac{\partial k}{\partial t}=\frac{\partial}{\partial y}\left(\frac{\nu_\mathrm{t}}{\sigma_k}\frac{\partial k}{\partial y}\right)-\frac{P_{kk}}{2}-\varepsilon,\tag{6}$$

while the turbulent energy dissipation rate ε depends on the choice of model. For the one-equation k–l model, ε is calculated from the empirical relationship[8]

$$\varepsilon=c_\mu^{3/4}k^{3/2}/\kappa y.\tag{7}$$

However, in the two-equation $k{-}\varepsilon$ model employed here, ε is calculated from its own transport equation

$$\frac{\partial\varepsilon}{\partial t}=\frac{\partial}{\partial y}\left(\frac{\nu_{\mathrm{t}}}{\sigma_\varepsilon}\frac{\partial\varepsilon}{\partial y}\right)-\frac{1}{2}(c_{\varepsilon1}P_{kk}-2c_{\varepsilon2}\varepsilon)\frac{\varepsilon}{k}. \tag{8}$$

The model constants are given in Table I.

The second scheme adopted here is based on the exact equation governing the transport of Reynolds stresses $\overline{u_iu_j}$. Consider the exact second-moment equations expressed in Cartesian tensor form as[20]

$$\begin{aligned}\underbrace{\frac{\mathrm{D}\overline{u_iu_j}}{\mathrm{D}t}}_{C_{ij}}=&-\underbrace{\left(\overline{u_iu_k}\frac{\partial U_j}{\partial x_k}+\overline{u_ju_k}\frac{\partial U_i}{\partial x_k}\right)}_{P_{ij}}+\underbrace{\frac{1}{\rho}(\overline{F_iu_j}+\overline{F_ju_i})}_{G_{ij}}\\ &-\underbrace{\frac{\partial}{\partial x_k}\left(\overline{u_iu_ju_k}+\overline{\frac{p}{\rho}(\delta_{jk}u_i+\delta_{ik}u_j)}-\nu\frac{\partial\overline{u_iu_j}}{\partial x_k}\right)}_{d_{ij}}\\ &+\underbrace{\overline{\frac{p}{\rho}\left(\frac{\partial u_i}{\partial x_j}+\frac{\partial u_j}{\partial x_i}\right)}}_{\phi_{ij}}-\underbrace{2\nu\overline{\frac{\partial u_i}{\partial x_k}\frac{\partial u_j}{\partial x_k}}}_{-e_{ij}}\end{aligned} \tag{9}$$

where F_i is a body force per unit mass. In accordance with tradition, equation (9) has been reduced to six distinct physical processes denoted by shorthand symbols corresponding to stress convection C_{ij}, production P_{ij}, body force interactions G_{ij}, diffusion d_{ij}, pressure-strain redistribution ϕ_{ij} and viscous dissipation ε_{ij}. Stress convection, production and (linear) body force effects may be treated as exact terms since they contain velocity correlations up to at most $\overline{u_iu_j}$. However, the remaining terms require alternative mathematical treatments in order to close the above exact equation. Beginning with d_{ij} which represents stress transport due to turbulent motions, the term can be conveniently subdivided into three processes corresponding to velocity-driven diffusion $\overline{u_iu_ju_k}$ due to fluctuating velocity components, pressure-driven diffusion $\overline{(p/\rho)(\delta_{jk}u_i+\delta_{ik}u_j)}$ through the action of pressure fluctuations and molecular diffusion $\nu\partial\overline{u_iu_j}/\partial x_k$. At high Reynolds numbers, molecular diffusion is assumed to be negligible and the *net* transport of the velocity- and pressure-driven processes is habitually modelled collectively. The model adopted for d_{ij} in the present work is the isotropic proposal of Shir:[21]

$$d_{ij}=\frac{\partial}{\partial x_k}\left(\frac{C_\mu}{\sigma_k}\frac{k^2}{\varepsilon}\frac{\partial\overline{u_iu_j}}{\partial x_k}\right). \tag{10}$$

The above model for d_{ij} supports the hypothesis that stress diffusion is driven by stress gradients. Note that equation (10) is not rotationally invariant, since the symmetry of the indices is not preserved on interchanging either i or j with k. However, the general belief is that the contribution of

Table I. Eddy viscosity model constants

κ	σ_k	σ_ε	$c_{\varepsilon1}$	$c_{\varepsilon2}$
0·4	1·0	1·3	1·45	1·92

the diffusive term to the stress budget is minimal and hence (10) is chosen on the basis of numerical convenience rather than accuracy.

The complex interaction of fluctuating strain and pressure, ϕ_{ij}, is an important process in equation (9) because it generally provides the main balance to the production terms. Since $\phi_{kk} = 0$, it is clear that the pressure–strain term serves to redistribute energy between all the stress components but does not alter the level of turbulent kinetic energy. The basic model employed in the present work is best interpreted by dividing the pressure–strain interaction into four distinct physical processes, i.e.

$$\begin{aligned}\phi_{ij} = {} & \underbrace{-c_1 \varepsilon a_{ij}}_{\phi_{ij1}} \; \underbrace{-c_2\left(P_{ij} - \tfrac{1}{3}\delta_{ij}P_{kk}\right)}_{\phi_{ij2}} \\ & + \underbrace{c_1^{\mathrm{w}}(\varepsilon/k)\left(\overline{u_k u_m} n_k n_m \delta_{ij} - \tfrac{3}{2}\overline{u_k u_i} n_k n_j - \tfrac{3}{2}\overline{u_k u_j} n_k n_i\right) f}_{\phi_{ij1}^{w}} \\ & + \underbrace{c_2^{\mathrm{w}}\left(\phi_{km2} n_k n_m \delta_{ij} - \tfrac{3}{2}\phi_{ik2} n_k n_j - \tfrac{3}{2}\phi_{jk2} n_k n_i\right) f}_{\phi_{ij2}^{w}} .\end{aligned} \tag{11}$$

Terms ϕ_{ij1} and ϕ_{ij2}, frequently referred to as the 'return-to-isotropy' and 'rapid' parts of the pressure–strain process, tend to isotropize the turbulent and mean fields respectively. Pressure reflections from the boundary are modelled by terms ϕ_{ij1}^{w} and ϕ_{ij2}^{w}. The model adopted in equation (11) is based on the proposal of Gibson and Launder.[22] The resultant wall 'echoing' is responsible for the transfer of the bed normal stress to bed parallel stresses and thus the process introduces a measure of near-bed stress anisotropy. The strength of the wall reflection terms is determined from the factor f, given by equation (31) below, which represents the ratio of the local length scale ($L \equiv k^{3/2}/\varepsilon$) to the normal distance from the bed, y. Terms n_i denote the unit vector normal to the bed, where $n_i = (0, 1, 0)$ for a flat bed. Craft and Launder[23] recently derived a new form for ϕ_{ij2}^{w} with special reference to impinging jets:

$$\begin{aligned}\phi_{ij2}^{\mathrm{w}} = -\Bigg[& 0{\cdot}08\frac{\partial U_l}{\partial x_m}\overline{u_l u_m}(\delta_{ij} - 3n_i n_j) - 0{\cdot}4k\frac{\partial U_l}{\partial x_m} n_l n_m (n_i n_j - 0{\cdot}33\delta_{ij}) \\ & + 0{\cdot}1k a_{lm}\left(\frac{\partial U_k}{\partial x_m}\delta_{ij} - 1{\cdot}5\frac{\partial U_i}{\partial x_m} n_l n_j - 1{\cdot}5\frac{\partial U_j}{\partial x_m} n_l n_j\right)\Bigg]\frac{k^{3/2}}{c_l \varepsilon y},\end{aligned} \tag{12}$$

where $c_l = 2{\cdot}5$ and a_{ij} is the dimensionless stress invariant given by

$$a_{ij} = \overline{u_i u_j}/k - \tfrac{2}{3}\delta_{ij}. \tag{13}$$

In practice the Craft and Launder[23] term has the effect of reducing the near-bed levels of k, $\overline{u^2}$ and $\overline{uv}$ whilst increasing the levels of $\overline{v^2}$, as was demonstrated by Sajjadi and Aldridge.[8]

At high-Reynolds-number turbulence the dissipation rate of turbulent energy can be assumed to be locally isotropic and thus we may write

$$\varepsilon_{ij} = \tfrac{2}{3}\delta_{ij}\varepsilon. \tag{14}$$

Following Launder *et al.*[20], ε is derived from its own transport equation

$$\frac{\partial \varepsilon}{\partial t} = \frac{\partial}{\partial y}\left(\frac{c_\varepsilon}{\sigma_\varepsilon}\frac{k^2}{\varepsilon}\frac{\partial \varepsilon}{\partial y}\right) + \frac{1}{2}(c_{\varepsilon 1}P_{kk} - 2c_{\varepsilon 2}\varepsilon)\frac{\varepsilon}{k}. \tag{15}$$

The model constants for the DSM closure model are given in Table II.

Table II. DSM model constants

C_μ	σ_k	σ_ε	c_ε	$c\varepsilon 1$	$c_{\varepsilon 2}$	c_1	c_2	c_1^{w}	c_2^{w}
0·065	0·81	1·0	0·15	1·45	1·92	1·8	0·6	0·5	0·3

The stress generation G_{ij} associated with rotation needs special treatment in DSM closure schemes. If the co-ordinate frame is rotated, an effective (linear) source term

$$G_{ij} - 2\Omega_k(\overline{u_j u_m}\varepsilon_{ikm} + \overline{u_i u_m}\varepsilon_{jkm}) \tag{16}$$

enters the Reynolds stress transport equations, where Ω_k is the co-ordinate rotation tensor and ε_{ijk} is the unit alternating tensor such that ε_{ijk} is $+1$ if ijk are in cyclic order, -1 if ijk are in anticyclic order and zero otherwise. In the present form the substantial convective derivative in equation (9) is not materially invariant under a rotation of axes. To circumvent this difficulty, we follow the suggestion of Takhar and Thomas[24] and incorporate half the rotation 'generation' in the convection term, i.e.

$$C'_{ij} \equiv \frac{\mathrm{D}\overline{u_i u_j}}{\mathrm{D}t} - \tfrac{1}{2}G_{ij}, \tag{17}$$

and the remaining part is added to the mean strain and rotational parts of ϕ_{ij}. We thus infer that

$$\phi'_{ij2} \equiv \phi_{ij2} + \phi_{ij3} = -c_2(P_{ij} + \tfrac{1}{2}G_{ij} - \tfrac{1}{3}\delta_{ij}P_{kk}), \tag{18}$$

since $G_{kk} = 0$, which implies that there is no direct turbulent energy created by the rotation. Note incidentally that this approach suggests that in applying the idea of isotropization of production to rotating systems, the effective generation associated with rotation is only half as great relative to shear generation as indicated by equation (9). Finally, following Launder *et al.*,[9] the pressure reflection term is modelled as

$$\phi^{\mathrm{w}}_{ij2} = c_2^{\mathrm{w}}(\phi'_{km2}n_k n_m \delta_{ij} - \tfrac{3}{2}\phi'_{ik2}n_k n_j - \tfrac{3}{2}\phi'_{jk2}n_k n_i)f. \tag{19}$$

3. NUMERICAL IMPLEMENTATION

The computational procedure for the governing transport equations is based on the fully conservative, collocated (non-staggered) finite volume framework such that all flow variables are stored at one and the same set of nodes. However, the implementation of second-moment closure models with such a scheme poses serious problems, particularly for models which are not based on the eddy viscosity concept. In the absence of eddy viscosity terms the collocated variable arrangement can cause decoupling of the mean velocity and Reynolds stresses, leading eventually to oscillatory solutions or even divergence of iterative solution algorithms. In the present paper the concept of apparent viscosity is adopted which circumvents the aforementioned Reynolds stress/mean velocity decoupling.

The transport equations governing the mean and turbulent fields may be cast in the form

$$\frac{\partial(\rho\phi)}{\partial t} - \frac{\partial}{\partial y}\left(\Gamma_\phi \frac{\partial\phi}{\partial y}\right) - S_\phi = 0. \tag{20}$$

In equation (20), ϕ represents any of the mean velocities, Reynolds stresses, turbulent kinetic energy or dissipation rate, Γ_ϕ is an isotropic diffusivity and S_ϕ contains all source/sink terms, including Reynolds stresses, mixed derivatives, constant pressure gradient terms (in the momentum equations) and Coriolis terms (see equations (38) and (39) below). Equation (19) is integrated over a control volume, as shown in Figure 1, which yields a balance of face fluxes and a volume-integrated net source.

In this scheme the transient term is approximated by the first-order one-sided difference simply to enable a time-marching solution. The cross-diffusion term is evaluated by bilinear interpolation, while the source term is discretized using single-point quadrature and is linearized as

$$S_\phi = S_\mathrm{P}\phi_\mathrm{P} + S_\mathrm{U}, \tag{21}$$

where S_P are contributions to the source term which are strictly positive. Integrating (20) gives

$$\rho[\theta\phi_\mathrm{P} + (1-\theta)\phi_\mathrm{P}^\mathrm{o}]\frac{\Delta y}{\Delta t} = \left(\Gamma_\phi\frac{\partial\phi}{\partial y}\right)_\mathrm{n} - \left(\Gamma_\phi\frac{\partial\phi}{\partial y}\right)_\mathrm{s} + S_\phi\Delta y. \tag{22}$$

Here $\phi_\mathrm{P}^\mathrm{o}$ is the value of ϕ_P at the previous time step and

$$\left(\Gamma_\phi\frac{\partial U}{\partial y}\right)_\mathrm{n} = \Gamma_\mathrm{n}\frac{\phi_\mathrm{N}-\phi_\mathrm{P}}{(\delta y)_\mathrm{n}}, \tag{23}$$

$$\left(\Gamma_\phi\frac{\partial U}{\partial y}\right)_\mathrm{s} = \Gamma_\mathrm{s}\frac{\phi_\mathrm{P}-\phi_\mathrm{S}}{(\delta y)_\mathrm{s}}. \tag{24}$$

Substituting (23) and (24) in (22), we obtain

$$\left(\rho\theta\frac{\Delta y}{\Delta t} + \frac{\Gamma_\mathrm{n}}{(\delta y)_\mathrm{n}} + \frac{\Gamma_\mathrm{s}}{(\delta y)_\mathrm{s}} - S_\mathrm{P}\Delta y\right)\phi_\mathrm{P} = \frac{\Gamma_\mathrm{n}}{(\delta y)_\mathrm{n}}\phi_\mathrm{N} + \frac{\Gamma_\mathrm{s}}{(\delta y)_\mathrm{s}}\phi_\mathrm{S} + S_\mathrm{U}\Delta y + (\theta-1)\frac{\Delta y}{\Delta t}\phi_\mathrm{P}^\mathrm{o}, \tag{25}$$

which may be expressed in the form

$$\left(A_\mathrm{N} + A_\mathrm{S} - S_\mathrm{P}\Delta y + \rho\theta\frac{\Delta y}{\Delta t}\right)\phi_\mathrm{P} = A_\mathrm{N}\phi_\mathrm{N} + A_\mathrm{S}\phi_\mathrm{S} + S_\mathrm{U}\Delta y + (\theta-1)\frac{\Delta y}{\Delta t}\phi_\mathrm{P}^\mathrm{o}. \tag{26}$$

Following Patankar,[16] we set $\theta = 1$, which ensures that the numerical scheme is fully implicit and therefore unconditionally stable regardless of the choice of the time step Δt. The resulting algebraic expression for ϕ yields a tridiagonal matrix equation of the form

$$A_\mathrm{P}\phi_\mathrm{P}^* = \sum_i A_i\phi_i^* + B, \quad i = \mathrm{N}, \mathrm{S}, \tag{27}$$

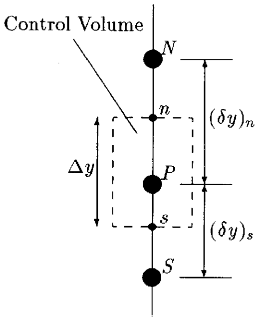

Figure 1. A typical control volume

where the coefficients are

$$\begin{aligned} &A_{\mathrm{N}}=\frac{\Gamma_{\mathrm{n}}}{(\delta y)_{\mathrm{n}}}, \qquad A_{\mathrm{S}}=\frac{\Gamma_{\mathrm{s}}}{(\delta y)_{\mathrm{s}}}, \qquad A_{\mathrm{P}}^{0}=\frac{\rho\Delta y}{\Delta t}-S_{\mathrm{P}}\Delta y, \\ &B=S_{\mathrm{U}}\Delta y, \qquad A_{\mathrm{P}}=A_{\mathrm{N}}+A_{\mathrm{S}}+A_{\mathrm{P}}^{0}. \end{aligned} \tag{28}$$

Face diffusivities are evaluated by linear interpolation using neighbouring nodes on either side of any face being considered. Since the grid is non-staggered, checkerboard oscillations arise if face velocities are linearly interpolated between related pairs of adjacent nodes. A correct treatment of cell face velocities is given in the next section; see equation (46).

4. NUMERICAL STABILITY

As mentioned in the previous section, the stability criterion is a serious difficulty in finite volume solvers, particularly those based on a fully collocated arrangement and non-diffusing discretization. The difficulty arises from the absence of eddy viscosity terms and a numerical decoupling of stresses from the related strains. This problem was first addressed by Lien and Leschziner,[15] who extracted apparent viscosities from the partial differential equations governing the transport of Reynolds stresses. To illustrate this technique, consider the $\overline{uv}$ transport equation which can be expressed as

$$C_{12}-d_{12}=-a-b+(P_{12}+\phi_{12}+a+b). \tag{29}$$

Terms a and b can be derived from the Reynolds stress equation represented in the general form

$$\rho\frac{\partial\Psi}{\partial t}-\frac{\partial}{\partial y}\left(s_{22}\frac{\partial\Psi}{\partial y}\right)=a_1P_{11}+a_2P_{22}+a_3P_{12}+a_4P_{kk}+\frac{\rho\varepsilon}{k}(a_5\overline{u^2}+a_6\overline{v^2}+a_7\overline{uv})+a_8\rho\varepsilon, \tag{30}$$

where Ψ denotes the Reynolds stress components and $s_{22}=c_sk^2/\varepsilon$. The coefficients a_i are given in Table III.

In Table III, $f_y=n_2^2f$, where

$$f=c_\mu^{3/4}k^{3/2}/\varepsilon\kappa y. \tag{31}$$

The spanwise Reynolds stress $\overline{w^2}$ is excluded from Table III since it is calculated through the relationship

$$\overline{w^2}=2k-(\overline{u^2}+\overline{v^2}). \tag{32}$$

Table III. Coefficients a_i in equation (30)

a_i	$\overline{u^2}$	$\overline{v^2}$	$\overline{uv}$
a_1	$1-c_2$	0	0
a_2	$-c_2c_2^{\mathrm{w}}f_y$	$1-c_2+2c_2c_2^{\mathrm{w}}f_y$	0
a_3	0	0	$1-c_2+\frac{3}{2}c_2c_2^{\mathrm{w}}f_y$
a_4	$\frac{1}{3}(c_2+c_2c_2^{\mathrm{w}}f_y)$	$\frac{1}{3}(c_2-2c_2c_2^{\mathrm{w}}f_y)$	0
a_5	$-c_1$	0	0
a_6	$c_1^{\mathrm{w}}f_y$	$-c_1-2c_1^{\mathrm{w}}f_y$	0
a_7	0	0	$-c_1-\frac{3}{2}c_1^{\mathrm{w}}f_y$
a_8	$\frac{2}{3}(c_1-1)$	$\frac{2}{3}(c_1-1)$	0

Apparent viscosities for the $\overline{uv}$ Reynolds shear stress component can be extracted from equation (29) by setting

$$a = \frac{\varepsilon}{k}(c_1 + \tfrac{3}{2}c_1^{\mathrm{w}}f_y)\overline{uv}, \tag{33}$$

$$b = (1 - c_2 + \tfrac{3}{2}c_2c_2^{\mathrm{w}}f_y)\overline{v^2}\frac{\partial U}{\partial y}. \tag{34}$$

Substituting (33) and (34) in (29) gives upon rearrangement

$$-\overline{uv} = \frac{k}{\varepsilon}\frac{C_{12} - d_{12} - (P_{12} + \phi_{12} + a + b)}{c_1 + \tfrac{3}{2}c_1^{\mathrm{w}}f_y} + \underbrace{\frac{k}{\varepsilon}\frac{1 - c_2 + \tfrac{3}{2}c_2c_2^{\mathrm{w}}f_y}{c_1 + \tfrac{3}{2}c_1^{\mathrm{w}}f_y}\overline{v^2}}_{\nu_{12}}\frac{\partial U}{\partial y}. \tag{35}$$

Apparent viscosities for the other Reynolds stress components can be derived following a path analogous to equations (29)–(35). The final result can be summarized as

$$\nu_{ij} = \begin{cases} \dfrac{1 - c_2 + \tfrac{3}{2}c_2c_2^{\mathrm{w}}(f_i + f_j)}{c_1 + \tfrac{3}{2}c_1^{\mathrm{w}}(f_i + f_j)}\dfrac{k\overline{u_j^2}}{\varepsilon} & \text{for } i \neq j, \\[2ex] \dfrac{2 - \tfrac{4}{3}c_2 + \tfrac{2}{3}c_2c_2^{\mathrm{w}}(f_i + f_j)}{c_1 + 2c_1^{\mathrm{w}}f_i}\dfrac{k\overline{u_i^2}}{\varepsilon} & \text{for } i = j \text{ (no summation)}. \end{cases} \tag{36}$$

In the above expression, f_i and f_j vary according to the value of i and j respectively:

$$f_i, f_j = \begin{cases} 1, & i, j = 2, \\ 0, & \text{otherwise}. \end{cases} \tag{37}$$

Insertion of the above viscosities ($\mu_{ij} = \rho\nu_{ij}$) into e.g. the momentum equation augments stability, since the cell face velocities also become functions of the normal stresses. Thus iteration into the U-momentum equation gives

$$\Gamma_U = \mu_{11}, \qquad S_U = -\frac{\partial P}{\partial x} - \frac{\partial}{\partial y}(\rho\overline{uv}) - 2\rho\Omega W, \qquad \rho\overline{uv} \leftarrow \rho\overline{uv} - \mu_{12}\frac{\partial U}{\partial y}. \tag{38}$$

Similarly, insertion into the W-momentum equation yields

$$\Gamma_W = \mu_{13}, \qquad S_W = -\frac{\partial P}{\partial z} - \frac{\partial}{\partial y}(\rho\overline{vw}) + 2\rho\Omega U, \qquad \rho\overline{vw} \leftarrow \rho\overline{vw} - \mu_{13}\frac{\partial W}{\partial y}. \tag{39}$$

Clearly the concept of apparent viscosities is only useful if the normal Reynolds stresses $\overline{u_i^2}$ remain positive at all times. This can be achieved through careful discrimination between positive and negative components of the source terms:

$$S_\phi = S_{\mathrm{U}} + S_{\mathrm{P}}\overline{u_i^2}, \tag{40}$$

where S_{U} contain positive terms while S_{P} accommodates strictly negative ones. Any term which does not contain $\overline{u_i^2}$ as a multiplier is first divided by the value of $\overline{u_i^2}$ available from the previous iteration level and then added to S_{P}. The product $S_{\mathrm{P}}\overline{u_i^2}$ is finally added to the main diagonal of the matrix in order to increase diagonal dominance and hence numerical stability.

As mentioned in the previous section, since the grid is collocated, checkerboard oscillations arise if a linear interpolation is used to approximate cell face velocities or Reynolds stresses in terms of nodal values. To overcome this difficulty, a non-linear interpolating scheme is used. For the purpose of illustration, consider the discretized form of the transport equation for $\overline{uv}$ at location P (see Figure 1):

$$\overline{uv}_{\mathrm{P}} = \underbrace{\frac{\sum_{i} A_i \phi_i + S'_{\mathrm{U}}}{A_{\mathrm{P}}}}_{H_{\mathrm{P}}/A_{\mathrm{P}}} + \frac{\mu^{\mathrm{P}}_{12}(U_{\mathrm{n}} - U_{\mathrm{s}})_{\mathrm{P}}}{\Delta y}, \quad i = \mathrm{N, S}, \tag{41}$$

where

$$\mu^{\mathrm{P}}_{12} = \left(\frac{1 - c_2 + \frac{3}{2} c_2 c^{\mathrm{w}}_2 f_y}{c_1 + \frac{3}{2} c^{\mathrm{w}}_1 f_y} \frac{k\overline{v^2}}{\varepsilon} \right)_{\mathrm{P}} \frac{\Delta y \Delta t}{A_{\mathrm{P}}}. \tag{42}$$

The term S'_{U} includes fragments of diffusion, production and the pressure–strain process. Analogous expressions for $\overline{uv}_{\mathrm{N}}$ and $\overline{uv}_{\mathrm{n}}$ are

$$\overline{uv}_{\mathrm{N}} = \frac{H_{\mathrm{N}}}{A_{\mathrm{N}}} + \frac{\mu^{\mathrm{N}}_{12}(U_{\mathrm{n}} - U_{\mathrm{s}})_{\mathrm{N}}}{\Delta y}, \tag{43}$$

$$\overline{uv}_{\mathrm{n}} = \frac{H_{\mathrm{n}}}{A_{\mathrm{n}}} + \frac{\mu^{\mathrm{n}}_{12}(U_{\mathrm{P}} - U_{\mathrm{N}})}{\Delta y}, \tag{44}$$

with

$$\mu^{\mathrm{n}}_{12} = \tfrac{1}{2}(\mu^{\mathrm{P}}_{12} + \mu^{\mathrm{N}}_{12}), \qquad \frac{H_{\mathrm{n}}}{A_{\mathrm{n}}} = \frac{1}{2}\left(\frac{H_{\mathrm{P}}}{A_{\mathrm{P}}} + \frac{H_{\mathrm{N}}}{A_{\mathrm{N}}}\right). \tag{45}$$

In equations (41) and (44) the north face velocity U_{n} is given by

$$\begin{aligned} U_n = {} & (1 - f^+_y)\left(\frac{A_{\mathrm{P}}}{A_{\mathrm{n}}}[U_{\mathrm{P}} - (1 - \alpha)U^*_{\mathrm{P}}] - \alpha \frac{\rho/\Delta t}{A_{\mathrm{n}}} U^{\mathrm{o}}_{\mathrm{P}}\right) \\ & + f^+_y \left(\frac{A_{\mathrm{N}}}{A_{\mathrm{n}}}[U_{\mathrm{N}} - (1 - \alpha)U^*_{\mathrm{N}}] - \alpha \frac{\rho/\Delta t}{A_n} U^{\mathrm{o}}_{\mathrm{N}}\right) \\ & + (1 - \alpha)U^*_n + \alpha \frac{\rho/\Delta t}{A_{\mathrm{n}}} U^{\mathrm{o}}_{\mathrm{n}}, \end{aligned} \tag{46}$$

with a similar expression for U_{s}. In equation (46), U^*_{P} represents the value of U_{P} at the previous iteration, α is the underrelaxation parameter and $f^+_y = (y_{\mathrm{n}} - y_{\mathrm{P}})/(y_{\mathrm{N}} - y_{\mathrm{P}})$. Equation (44) becomes

$$\overline{uv}_{\mathrm{n}} = \underbrace{\tfrac{1}{2}(\overline{uv}_{\mathrm{P}} + \overline{uv}_{\mathrm{N}})}_{\text{linear interpolation}} + \underbrace{\frac{1}{2\Delta y}[(\mu^{\mathrm{P}}_{12} + \mu^{\mathrm{N}}_{12})(U_{\mathrm{P}} - U_{\mathrm{N}}) - \mu^{\mathrm{P}}_{12}(U_{\mathrm{n}} - U_{\mathrm{s}})_{\mathrm{P}} - \mu^{\mathrm{N}}_{12}(U_{\mathrm{n}} - U_{\mathrm{s}})_{\mathrm{N}}]}_{\text{non-linear smoothing,}} \tag{47}$$

with an analogous expression for $\overline{uv}_{\mathrm{s}}$. The above practice of extracting apparent viscosities is to enhance iterative stability by increasing the magnitude of the diagonal coefficient A_{P}. To generalize the practice to unsteady flow and include underrelaxation, (47) is further modified as

$$\begin{aligned}\overline{uv}_{\mathrm{n}} = {} & \frac{1}{2}\left(\frac{A_{\mathrm{P}}}{A_{\mathrm{n}}}\overline{uv}_{\mathrm{P}} + \frac{A_{\mathrm{N}}}{A_{\mathrm{n}}}\overline{uv}_{\mathrm{N}}\right) + (1-\alpha)\left[\overline{uv}_{\mathrm{n}} - \frac{1}{2}\left(\frac{A_{\mathrm{P}}}{A_{\mathrm{n}}}\overline{uv}_{\mathrm{P}} + \frac{A_{\mathrm{N}}}{A_{\mathrm{n}}}\overline{uv}_{\mathrm{N}}\right)\right] \\ & + \alpha\,\frac{(\rho\Delta y/\Delta t)_{\mathrm{n}}\overline{uv}_{\mathrm{n}}^{0} - \frac{1}{2}[(\rho\Delta y/\Delta t)_{\mathrm{P}}\overline{uv}_{\mathrm{P}}^{0} + (\rho\Delta y/\Delta t)_{\mathrm{N}}\overline{uv}_{\mathrm{N}}^{0}]}{A_{\mathrm{n}}} \\ & + \alpha\left[\mu_{12}^{\mathrm{n}}\frac{U_{\mathrm{P}} - U_{\mathrm{N}}}{\Delta y} - \frac{1}{2}\left(\mu_{12}^{\mathrm{P}}\frac{(U_{\mathrm{n}} - U_{\mathrm{s}})_{\mathrm{P}}}{\Delta y} + \mu_{12}^{\mathrm{N}}\frac{(U_{\mathrm{n}} - U_{\mathrm{s}})_{\mathrm{N}}}{\Delta y}\right)\right]. \qquad (48)\end{aligned}$$

5. BOUNDARY CONDITIONS

The turbulence models presented in Section 2 are based on the key assumption that the local Reynolds number $R_{\mathrm{t}}(\equiv k^2/\nu\varepsilon)$ remains high over the entire flow domain. Inevitably there are near-bed, semiviscous flow regions which damp turbulence significantly and thus reduce R_{t}. Such regions must therefore be bridged via an alternative model. To date, many workers[1,4,17] have integrated the transport equations straight to the bed and applied the no-slip condition at a suitable roughness height Z_0. To implement this strategy, it is argued that for rough boundary layer flows the near-bed, semiviscous region is so thin in comparison with the roughness element that it does not influence the flow field. For example, Aldridge[17] set $z_0 = 2/3d + k_{\mathrm{s}}/30$, where d is the sand grain diameter and k_{s} is the Nikuradse sand grain roughness. However, in the context of oscillatory boundary layer flows (over a rough or a smooth surface) the flow does not always remain fully turbulent in all phases of oscillation, particularly around flow reversal and during the early stages of flow acceleration.[11,18] This fact seriously questions the validity of the traditional boundary conditions. Therefore in the present work this approach is abandoned in favour of the roughness-dependent wall function approach originally proposed by Sajjadi and Aldridge.[8] This approach explicitly takes into account the nature of the flow at the bed (be it hydraulically smooth, transitional or fully rough).

The present wall function approach relies on the assumption that the near-wall region lying between the wall and the near-wall computational node N is represented by two layers. The lower one is a fully viscous region and the upper one is a fully turbulent layer where the velocity profile has the form

$$U = \frac{U_\tau}{\kappa}\ln\left(\frac{y}{y_0}\right), \qquad (49)$$

where $\kappa = 0{\cdot}4$ is the von Karman constant, $U_\tau = (\tau_{\mathrm{w}}/\rho)^{1/2}$ is the friction velocity and τ_{w} represents the wall shear stress. The vertical distance y is taken from the base of the sand grains and the parameter y_0 is determined by the state of the bed roughness. If the velocity scale in the log-law region is proportional to $k^{1/2}$, the form of y_0 is given by

$$y_0 = \mu/E\rho c_\mu^{1/4}k^{1/2} \qquad (50)$$

The roughness parameter E varies according to the state of the bed roughness[25] and is evaluated following Krishnappen[26] by the expression

$$E = \exp(\kappa B_{\mathrm{s}})/k_{\mathrm{s}}^{+}, \qquad (51)$$

where $k_s^+ = U_\tau k_s/\nu$. Here B_s is determined empirically through the relationship

$$B_s(k_s^+) = (5{\cdot}5 + 2{\cdot}5 \ln k_s^+) \exp[-0{\cdot}062(\ln k_s^+)^3] + 8{\cdot}5\{1 - \exp[-0{\cdot}062(\ln k_s^+)^3]\}, \tag{52}$$

which represents an excellent fit to the experimental data of Nikuradse[27] as was originally demonstrated by Sajjadi and Aldridge.[8] The value of turbulent kinetic energy at the wall is governed by the balance between volume-integrated production and dissipation. It must be evaluated in a manner consistent with the log-law variation in the cell. If the point N is assumed to be in the log-law region, then the wall shear stress may be expressed as

$$\boldsymbol{\tau}_w = \frac{\rho k_N^{1/2} C_\mu^{1/4} \kappa}{\ln(E y k_N^{1/2} \nu)} \mathbf{U}. \tag{53}$$

Near the wall the coefficient C_μ is obtained from the modelled Reynolds stress equations, by assuming local equilibrium and setting $f_y = 1$, as

$$C_\mu = \frac{1 - c_2 + \frac{3}{2} c_2 c_2^w}{c_1 + \frac{3}{2} c_1^w} \frac{\overline{v_N^2}}{k_N} = 0{\cdot}065. \tag{54}$$

The value of turbulent kinetic energy in the wall-neighbouring control volumes is calculated by introducing the same assumptions in its transport equation, with the modification that the diffusion to the wall is set to zero, i.e. $(\partial k/\partial y)_s = 0$.

However, a different methodology is applied for the near-wall values of Reynolds stresses. The treatment adopted here involves prescribing the value of all stresses at the near-wall node. Following Lien and Leschziner,[15] values for Reynolds stresses are derived by focusing on the stress equations applicable to local equilibrium, $P_{kk} = 2\rho\varepsilon$, and setting the wall distance function $f = 1$. Thus we obtain

$$\widehat{\overline{u^2}} = \frac{k(4c_1 + 2c_1^2 - 4c_1 c_2 + 2c_1 c_2 c_2^w + 6c_1^w + 6c_1 c_1^w - 6c_1^w c_2)}{3c_1(c_1 + 2c_1^w)} = 1{\cdot}098k,$$

$$\widehat{\overline{v^2}} = \frac{2k(c_1 + c_2 - 2c_2 c_2^w - 1)}{3(c_1 + 2c_1^w)} = 0{\cdot}247k,$$

$$-\widehat{\overline{uv}} = k\sqrt{\left(\frac{1 - c_2 + \frac{3}{2} c_2 c_2^w}{c_1 - \frac{3}{2} c_1^w} \frac{2(c_1 + c_2 - 2c_2 c_2^w - 1)}{3(c_1 + 2c_1^w)}\right)} = 0{\cdot}255k,$$

where, for example, $\widehat{\overline{uv}}$ is the value of the Reynolds shear stress at the wall.

Finally, the near-wall dissipation is not obtained from the solution of its transport equation in the bed-adjacent node. Instead, a treatment consistent with the log-law assumption is made which involves the evaluation of ε_N from

$$\varepsilon_N = c_\mu^{3/4} k_N^{3/2} / \kappa y_N. \tag{55}$$

At the top boundary the following conditions are applied:

$$\frac{\partial U}{\partial y} = \frac{\partial W}{\partial y} = \frac{\partial k}{\partial y} = \frac{\partial \varepsilon}{\partial y} = \frac{\partial \overline{u^2}}{\partial y} = \frac{\partial \overline{v^2}}{\partial y} = \overline{uv} = 0. \tag{56}$$

However, for the rectilinear tidal flow calculations a wind-free surface condition for ε is applied according to the proposal made by Rodi:[28]

$$\varepsilon(H,t)=\frac{(kc_\mu^{1/2})^{3/2}}{\kappa(H-y+\beta H)}. \tag{57}$$

In equation (57), H is the water depth and $\beta = 0{\cdot}07$ is an empirical constant determined by Hossain.[29] Furthermore, following McClean,[7] it is assumed that the pressure in the momentum equations is replaced by the free surface elevation η according to

$$\frac{\mathrm{d}\eta}{\mathrm{d}x}=-\rho g S_{\max}\cos(\omega t), \tag{58}$$

where $g = 9{\cdot}81\ \mathrm{m\,s^{-2}}$ denotes the gravitational acceleration and $S_{\max}$ is the maximum surface slope.

Initial conditions for the mean and turbulent variables are all set to zero and the calculations are performed over five tidal cycles in order to ensure that the flow has reached the fully periodic state.

6. RESULTS

6.1. Comparisons with Rectilinear Tidal Flows; $W = 0$

In general the influence of the Earth's rotation cannot be neglected in tidal flow problems. However, in an initial series of calculations presented here we will consider two rectilinear tidal problems which neglect the effects of rotation. This situation may be approximated in a narrow channel or an estuary where the tidal motion is reduced to one direction only and a second perpendicular, co-planar mean velocity cannot develop. In this subsection we compare both linear eddy viscosity and DSM models with the experimental data of Schröder[6] (Elbe estuary) and McClean[7] (Jade estuary). The important experimental parameters are presented in Table IV.

Here the Reynolds number $Re = U_\infty H/\nu$ is based on the current velocity U_∞, the water column depth H and the kinematic viscosity of the fluid, ν. Furthermore, $S_{\max}$ denotes the maximum surface slope, while d is the roughness diameter of the particles.

6.1.1. Model comparisons with Jade estuary experimental data. Since the numerical scheme is fully implicit in time, the stability of the scheme is guaranteed regardless of the time step. In all the presented rectilinear tidal calculations the period was $T = 12{\cdot}42$ h and the time step increment was set to $\Delta t = 75$ s, while the number of grids in the vertical direction was $N = 60$. The grid spacing was based on a geometric progression with geometric ratio $r_\mathrm{c} = 1{\cdot}04$ such that close to the bed the mesh was tightly packed. This was motivated by the presence of sharp gradients in the near-bed region which require a high mesh line density in order to be resolved adequately.

The Nikuradase roughness length was set to $k_\mathrm{s} = 5 \times 10^{-3}$ m, the same value used in the k–ε predictions of Baumert and Radach.[5] This value was calculated from the approximate empirical relationship $k_\mathrm{s} = 2{\cdot}5d$ corresponding to a roughness diameter of $d = 0{\cdot}2$ cm.

Figure 2(a) compares eddy viscosity predictions for normalized current velocity profiles $U/U_{\max}$ (measured at $h \approx 2{\cdot}14$ m above the estuary bed) against normalized time t/T based on an arbitrary

Table IV. Experimental data for rectilinear tidal flows

Estuary	$S_{\max}$	d (cm)	U_∞ ($\mathrm{m\,s^{-1}}$)	H (m)	Re
Elbe[6]	5×10^{-5}	2	0·94	5·1	5×10^{6}
Jade[7]	2×10^{-5}	0·2	1·07	20	$2{\cdot}2\times10^{7}$

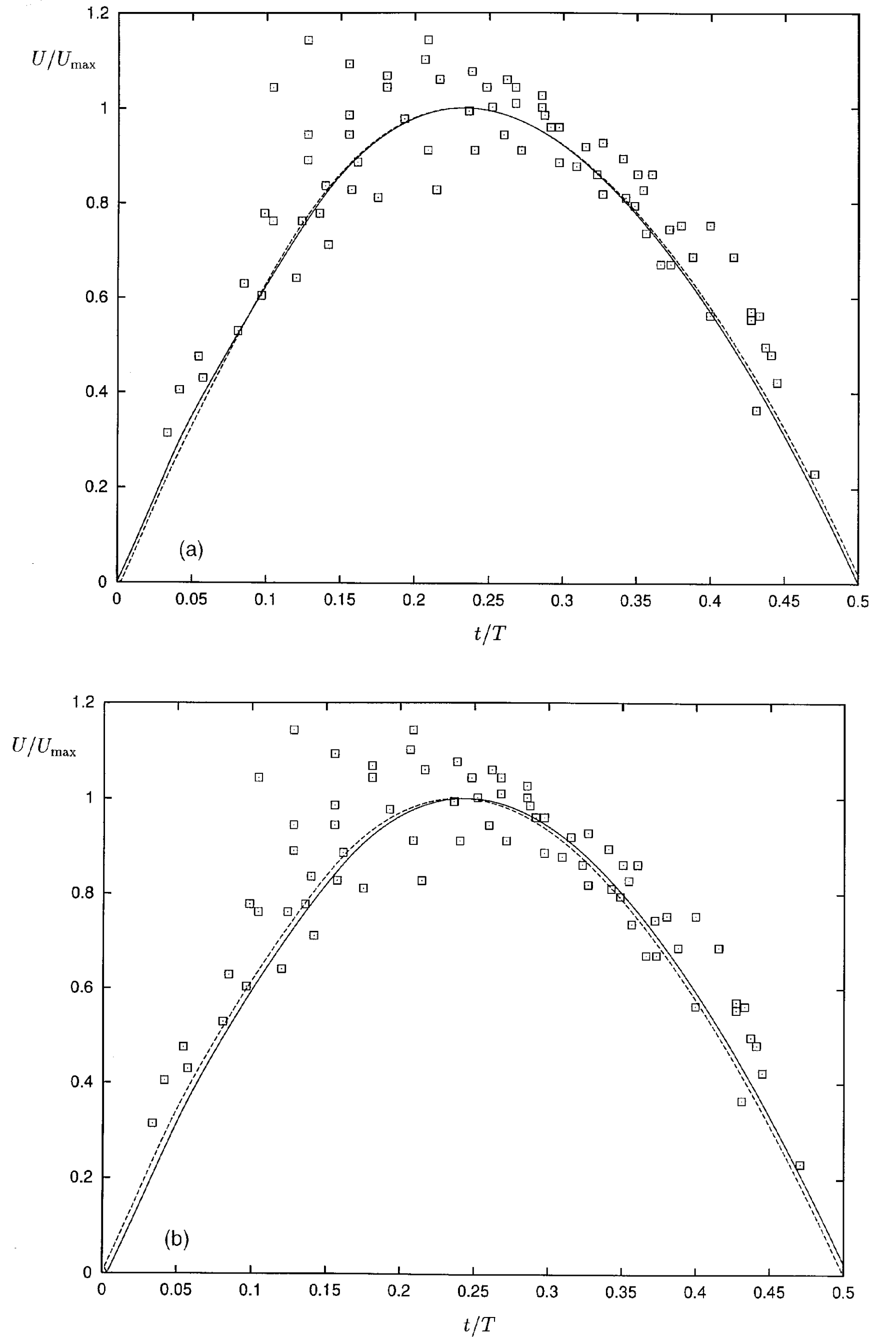

Figure 2. Normalized current velocity predictions of Jade estuary: (a) —, k–l; – – –, k–ε; (b) —, DSM-IP; – – –, DSM-CL; ⊡, experimental data of McClean[7] measured at $h \approx 2{\cdot}14$ m above bed of estuary

time axis with the experimental data of McClean.[7] The term $U_{\max}$ corresponds to the maximum velocity of the fluid at $h \approx 2{\cdot}14$ m above the bed along the half-cycle. We note that the eddy viscosity predictions are in excellent agreement with experimental data along the range $0 \leqslant t/T \leqslant 0{\cdot}5$, capturing the maximum at $t/T \approx 0{\cdot}25$ very closely. Figure 2(b) compares the same experimental data with DSM predictions for normalized current velocity against normalized time, once more represented on an arbitrary time axis. The distinction between the DSM models is based on the choice of the pressure–strain term ϕ^{w}_{ij2}. For brevity, computed DSM values which employ the Gibson and Launder[22] proposal (equation (11)) will herein be referred to as the DSM-IP model. Similarly, DSM results which apply the Craft and Launder[23] term (equation (12)) will be denoted by DSM-CL. The DSM proposals capture the experimental profile closely, including the maximum positioned at $t/T \approx 0{\cdot}25$, around which time the velocity at the free surface is also at its maximum value.

Experimental predictions of the normalized turbulent stress $\tau/\tau_{\max}$ (again measured at $h \approx 2{\cdot}14$ m above the Jade estuary bed) are compared with eddy viscosity and DSM models in Figures 3(a) and 3(b) respectively, where the abscissa represents a normalized time scale plotted on an arbitrary time axis. Here τ is based on the Reynolds shear stress, $\tau = -\rho\overline{uv}$, and $\tau_{\max}$ denotes the maximum value of τ across the range $0{\cdot}0 \leqslant t/T \leqslant 0{\cdot}5$ at height $h \approx 2{\cdot}14$ m. We note excellent agreement with experimental observations particularly in the vicinity of the maximum value of $\tau/\tau_{\max}$. Also, the time difference (or time lag) between the experimental current velocity and Reynolds shear stress profiles, estimated to be 1 h at flow reversal, is captured satisfactorily by all models. Minor improvements are noted for the DSM predictions in the time range $0{\cdot}0 \leqslant t/T \leqslant 0{\cdot}25$. However, it is inevitable that the experimental data presented in Figures 2 and 3 have been measured a considerable distance away from the bed. Therefore, although the above predictions are very good, no firm conclusions can be made concerning the relative strength of the turbulence models.

For the remainder of this subsection we will concentrate on mean and turbulent field predictions by the DSM-IP and DSM-CL models over the time range $0 \leqslant t \leqslant 5{\cdot}69$ h. For convenience this time range is subdivided into two tidal stages corresponding to (a) the first acceleration stage $0 \leqslant t \leqslant 2{\cdot}59$ h and (b) the first deceleration stage $3{\cdot}11 < t \leqslant 5{\cdot}69$ h. The acceleration and deceleration stages are also divided into six time stations which display the time instant (in hours) under consideration.

Current velocity profiles U predicted by the DSM models show during the first acceleration stage that the boundary layer is initially small but grows. However, it is unclear whether the boundary layer is fully developed or not during the late time stations of the first acceleration stage. Differences between the DSM-IP and DSM-CL models are only significant during the early time stations of the first acceleration stage, whereas during the late time stations of the acceleration stage they are small. After pressure gradient reversal (at $t \approx 3{\cdot}1$ h) the current velocity profiles begin to decelerate and again minor differences between the DSM models develop.

From predictions for Reynolds shear stress profiles we see that in the first acceleration stage the turbulence builds up sharply in the near-bed region owing to shear layer instability[30,31] and is constantly diffused upwards towards the free surface. At $t = 3{\cdot}11$ h we note an almost linear variation in $-\rho\overline{uv}$ along the entire depth, as was noted earlier by Davies and Jones.[1] This is in direct contrast with high-frequency waves driving the flow (e.g. wind waves of period $T = 8-10$ s), where the Reynolds shear stress decays rapidly as the freestream region is approached.[1,11] This suggests that the diffusion process for tidal flows is more dominant that observed in wind wave simulations. In the time range $2{\cdot}07 \leqslant t \leqslant 5{\cdot}69$ h it is clear that significant levels of turbulent energy are present in the vicinity of the free surface, suggesting that the turbulent boundary layer is not fully developed in this time interval. During the first deceleration stage the increasingly adverse pressure gradient destroys turbulent energy, eventually leaving it evenly dispersed along the depth of the estuary at the final time frames.

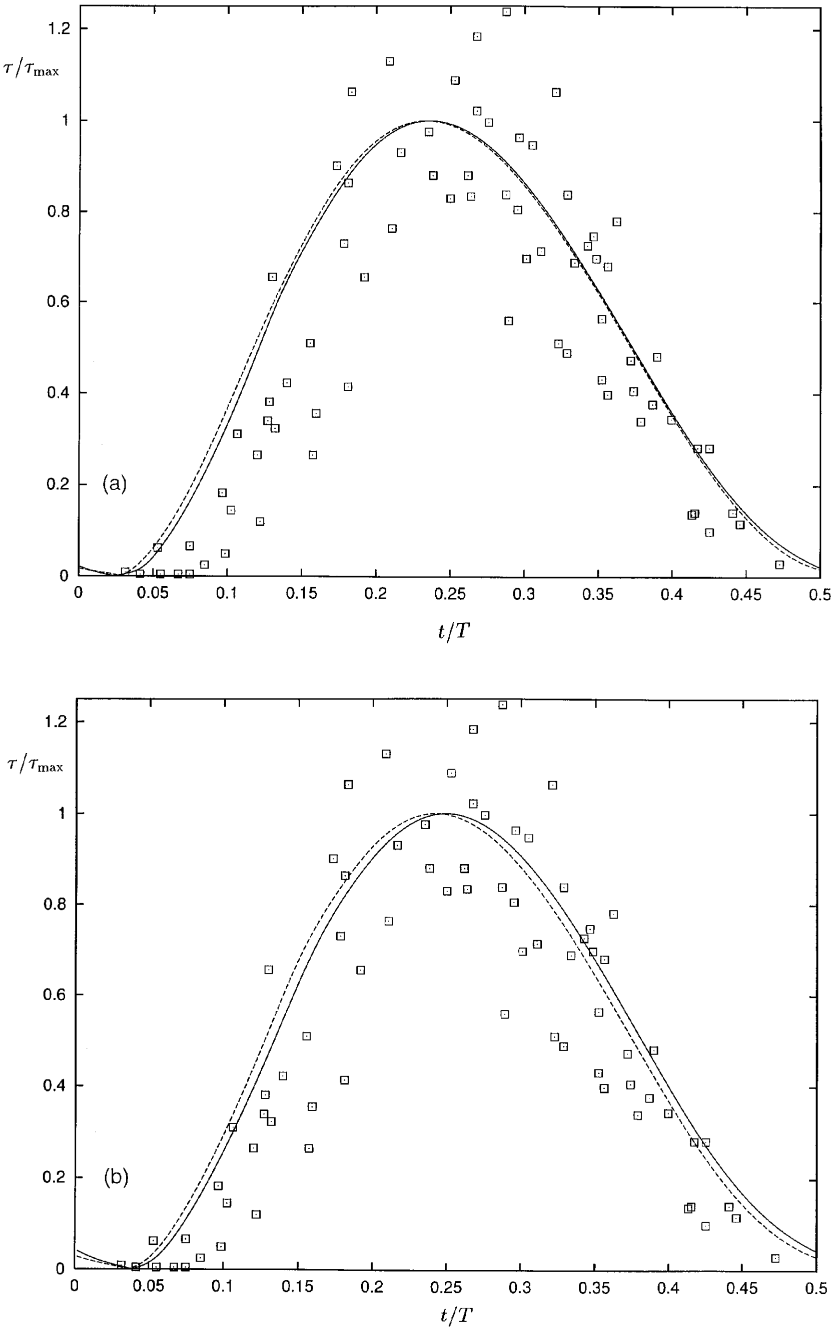

Figure 3. Normalized turbulent stress predictions of Jade estuary: (a) —, k–l; – – –, k–ε; (b) —, DSM-IP; – – –, DSM-CL; ⊡, experimental data of McClean[7] measured at $h \approx 2{\cdot}14$ m above bed of estuary

Turbulent kinetic energy predictions for the DSM-IP and DSM-CL models across the half-cycle are presented in Figures 4(a) and 4(b). The figures are a good example of the near-bed build-up of turbulent energy and its constant diffusion towards the free surface observed during the acceleration stage of tidal flows. With the onset of pressure gradient reversal the initial time frames of the deceleration stage indicate that high near-bed energy levels are sustained owing to the turbulence-bursting phenomenon,[13] leading to hysteresis in the turbulent energy cycle.[12] Furthermore, the

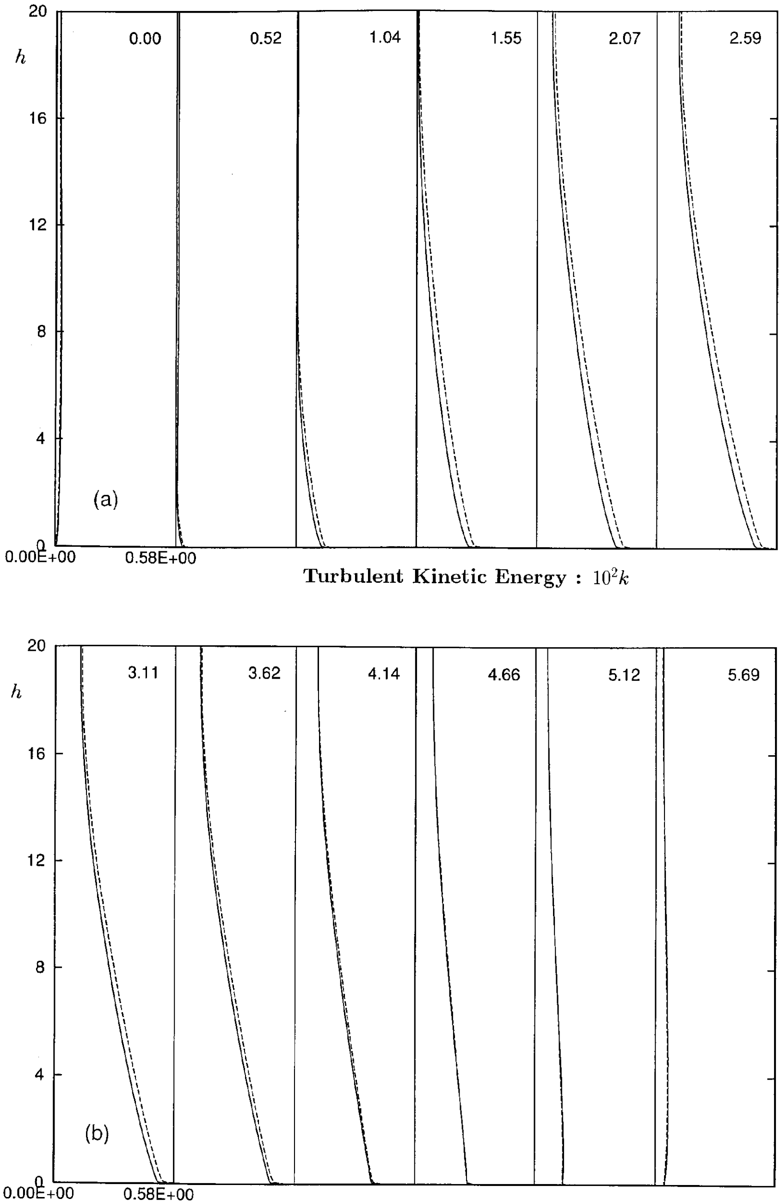

Figure 4. Turbulent kinetic energy predictions along height of Jade estuary: (a) first acceleration stage; (b) first deceleration stage; —, DSM-IP; – – –, DSM-CL

variation in the k profiles at these time stations between the bed and free surface is approximately linear. However, as the pressure gradient becomes increasingly adverse, turbulent kinetic energy is dissipated until at $t \approx 5{\cdot}69$ h it becomes evenly diffused through the depth of the estuary. In addition, we note that high levels of turbulent energy are not recorded across the entire half-cycle. This is probably due to the very small sand grain diameter, $d = 0{\cdot}2$ cm, which does not induce enough drag for the flow to remain fully turbulent at all time stations of the half-cycle.

Computed values of the normal Reynolds stresses $\overline{u^2}$, $\overline{v^2}$ and $\overline{w^2}$ show that each Reynolds stress component follows the salient trends of the turbulent kinetic energy, including (a) the build-up of energy in the near-bed region during the first acceleration stage and (b) its dissipation during the first deceleration stage, eventually becoming evenly diffused along the cross-section of the estuary. Predictions for $\overline{u^2}$ by the DSM-IP and DSM-CL models are in general very similar. However, we note that during the late time stations of the first acceleration stage the DSM-CL model predicts approximately three times as much near-bed component energy for $\overline{v^2}$ as the DSM-IP model. Conversely, the DSM-IP model predicts approximately twice as much near-bed component energy for $\overline{w^2}$ as the DSM-CL simulation. This is consistent with the observations of Waywell and Sajjadi,[18] who noted that the Craft and Launder[23] pressure–strain wall reflection term ϕ^{w}_{ij2} directed more energy to $\overline{v^2}$ (mainly from $\overline{w^2}$) compared with the predictions of the Gibson and Launder[22] proposal.

6.1.2. Model comparisons with Elbe estuary experimental data. Schröder's[6] experimental current velocity profiles measured at $h \approx 1{\cdot}9$ m are plotted against time and compared with linear eddy viscosity and DSM predictions in Figures 5(a) and 5(b). Note that once again the time axis is arbitrary. Although comparisons between numerical results and experimental data are good, it is interesting to note that the three maxima observed in the experimental predictions occur at different magnitudes, largely owing to the higher-order tidal harmonics observed in naturally occurring tides. This is in contrast with the eddy viscosity predictions, where all maxima are of equal size. Since the present simulations are forced only with the semidiurnal harmonic D_2 of period $t \approx 30^\circ\,\mathrm{h}^{-1}$, large discrepancies are noted in some parts of the flow cycle, particularly around $t = 12-14$ h.

Variations in turbulent kinetic energy against time for the linear eddy viscosity and DSM models and experimental data (again measured at $h \approx 1{\cdot}9$ m above the estuary bed) are compared in Figures 6(a) and 6(b). The experimental data again demonstrate three maxima of varying size, a feature which remains unresolved by the eddy viscosity models. Nevertheless, comparisons between experimental data and eddy viscosity predictions are satisfactory. Here we note that the present $k-\varepsilon$ predictions are similar to the $k-\varepsilon$ simulations of Baumert and Radach.[5] Furthermore, the time lag between the current profiles and turbulent kinetic energy predictions observed around flow reversal is also well reproduced by all models and is again estimated to be approximately 1 h.

We next consider the variation in the normal Reynolds stress components with time (again recorded at $h \approx 1{\cdot}9$ m above the estuary bed). Beginning with the DSM-IP predictions, we note that along the flow cycle the dominant Reynolds stress is $\overline{u^2}$, followed by $\overline{w^2}$ and then $\overline{v^2}$. Again the DSM-IP model predicts the maxima at the same height throughout the time cycle, since the flow is driven only by semidiurnal harmonic forcing. Compared with the DSM-IP model, the DSM-CL model predicts similar levels of $\overline{u^2}$ along the time cycle. Significant differences arise, however, in the DSM-CL predictions of $\overline{v^2}$ and $\overline{w^2}$, which remain at similar levels at all times during the DSM-CL simulation. It appears that the DSM-CL model increases the $\overline{v^2}$ distribution by extracting component energy from $\overline{w^2}$. Similar pressure–strain mechanics was observed for the Jade estuary calculations. Furthermore, like the comparisons with experimental data from the Jade estuary (Figures 2 and 3), the model parameters were not tuned and are not in fact identical to those employed in previous wind wave numerical simulations.[11,18]

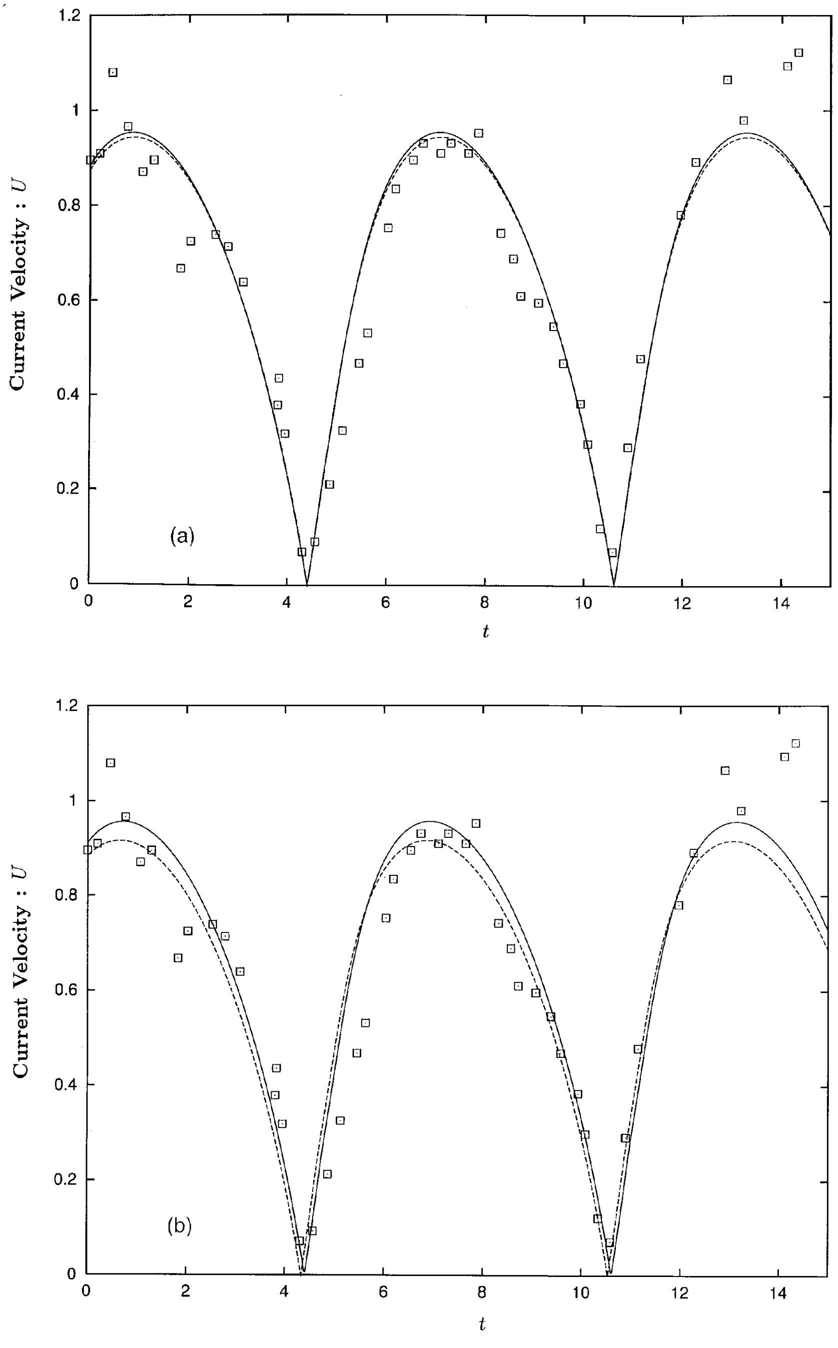

Figure 5. Current velocity predictions of Elbe estuary: (a) —, $k-l$; ---, $k-\varepsilon$; (b) —, DSM-IP; ---, DSM-CL; ⊡, experimental data of Schröder[6] meeasured at $h \approx 1{\cdot}9\,\mathrm{m}$ above bed of estuary

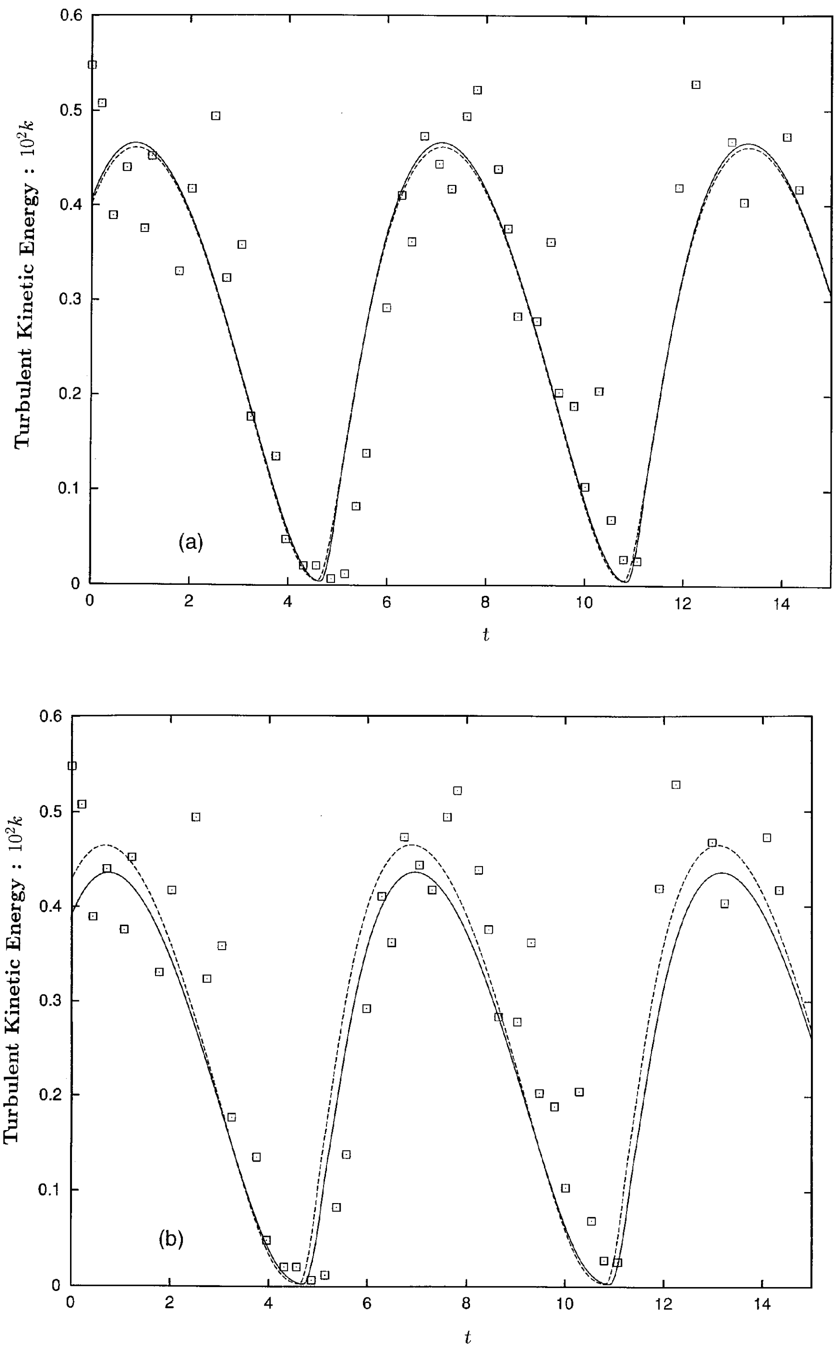

Figure 6. Turbulent kinetic energy predictions of Elbe estuary: (a) —, k–l; ---, k–ε; (b) —, DSM-IP; ---, DSM-CL; ⊡, experimental data of Schröder[6] measured at $h \approx 1{\cdot}9$ m above bed of estuary

From current velocity profiles predicted by the DSM models through the depth of the Elbe estuary, like the Jade estuary (Figure 3), it is unclear whether the turbulent boundary layer is fully developed when it reaches the free surface. Also noteworthy are minor differences between DSM-IP and DSM-CL predictions along the time range.

Predictions for Reynolds shear stress profiles show high-shear layers in the near-bed region where most of the turbulence is generated. During the fully turbulent time stations ($0 \leqslant t \leqslant 2{\cdot}07$ h and $6{\cdot}21 \leqslant t \leqslant 8{\cdot}28$ h) the Reynolds shear stress profiles vary linearly along the length of the estuary. This feature was also observed in the numerical simulations of Davies and Jones.[1] Furthermore, the DSM-CL model predicts greater shear stress levels in the near-bed region than the DSM-IP model.[11,18]

Results for turbulent kinetic energy profiles show that the highest levels of turbulent energy are generated at the bed and are continually diffused upwards towards the free surface. The figures also indicate that apart from the time frames $t = 4{\cdot}14$ and $10{\cdot}35$ h the Elbe estuary retains high levels of turbulent energy for the majority of the flow cycle.

Minor discrepancies between the DSM models are noted away from the bed, where the DSM-CL model predicts greater levels of turbulent energy than the DSM-IP results. This trend was also observed in the Jade estuary turbulent kinetic energy predictions in Figure 4.

6.2. DSM-IP predictions of a circular tidal flow; $\Omega = 6 \times 10^{-5}$ s^{-1}

The effect of the Earth's rotation cannot in general be neglected in tidal flow calculations. In open sea regions one must solve the coupled system of partial differential equations given by (1), introducing a second current velocity W which lies in the same two-dimensional plane as U. In the analysis below we compare DSM-IP predictions for a circular tidal flow with a numerical simulation previously reported by Davies,[4] who applied the one-equation k–l model as well as two modal models to the same tidal problem. In the same paper the no-slip current velocity boundary condition was set at the roughness length Y_0. The important parameters for the circular tide simulation are given in Table V.

In the present simulations a value for d (and hence $k_s = 2{\cdot}5d$) was evaluated through the empirical relationship $Y_0 = \frac{2}{3}d + k_s/30$.[17] In addition, a phase difference between the forcing motions was assumed, namely the W-current forcing led the U-current forcing by $\Phi = 45°$. It was further assumed that the tidal period was $T = 12$ h. Beginning with the current velocity profiles, Figure 7 presents DSM-IP predictions for U plotted along the depth of the estuary, h, across the flow cycle $0 \leqslant t \leqslant 11$ h, subdivided into (a) the first half-cycle $0 \leqslant t \leqslant 5$ h and (b) the second half-cycle $6 \leqslant t \leqslant 11$ h. Like the rectilinear simulations, it is unclear whether the turbulent boundary layer is fully developed or not during the entire flow cycle. It is evident, however, that at the free surface the U-velocity is very close to its freestream value $U_\infty = 1{\cdot}0$ m s^{-1}. Figures 8(a) and 8(b) display the W-current velocity profiles plotted against depth along the flow cycle. The W-velocity boundary layer extends up to the free surface, just exceeding its freestream value there, $W_\infty = 1{\cdot}0$ m s^{-1}.

Table V. Parameters for circular tidal flow test case

U_∞ (m s^{-1})	W_∞ (m s^{-1})	H (m)	Y_0 (m)
1·0	1·0	10	0·01

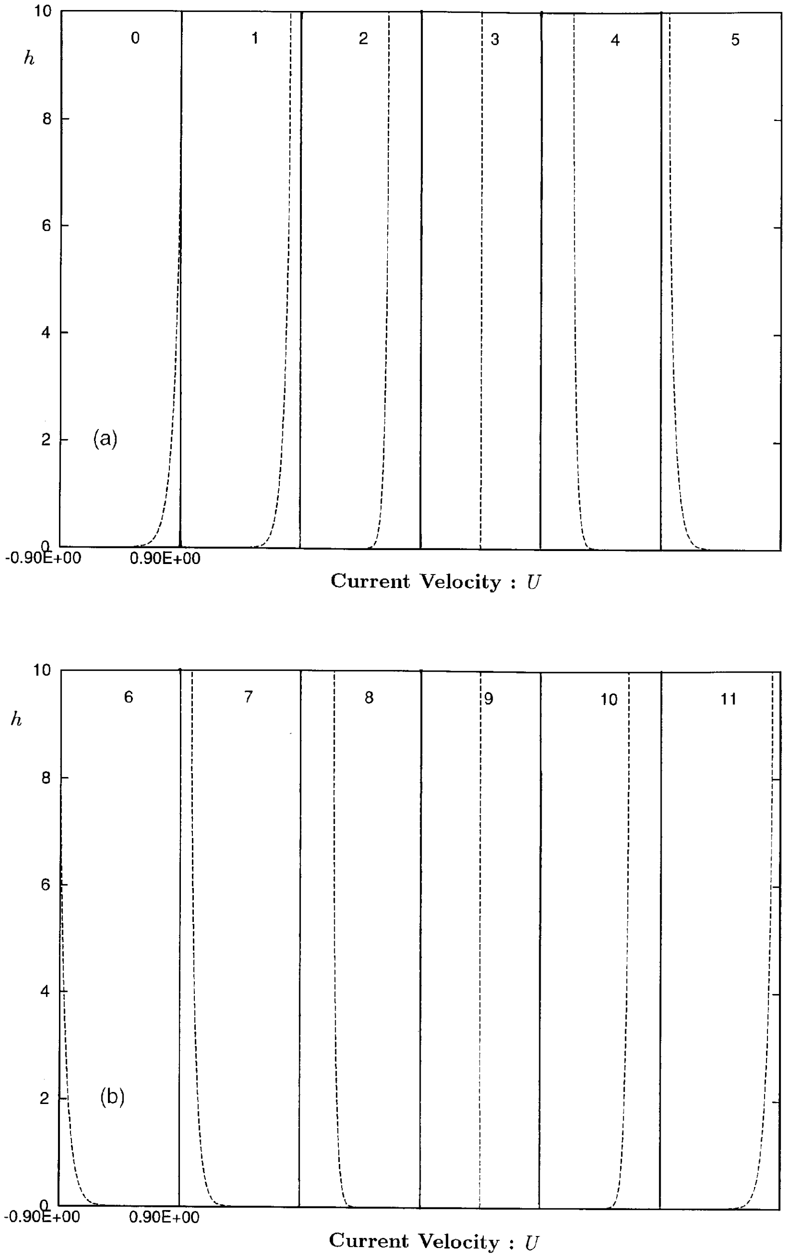

Figure 7. Streamwise current velocity predictions U along height of simulated open sea region across flow cycle $0 \leqslant t \leqslant 11$ h: ---, DSM-IP

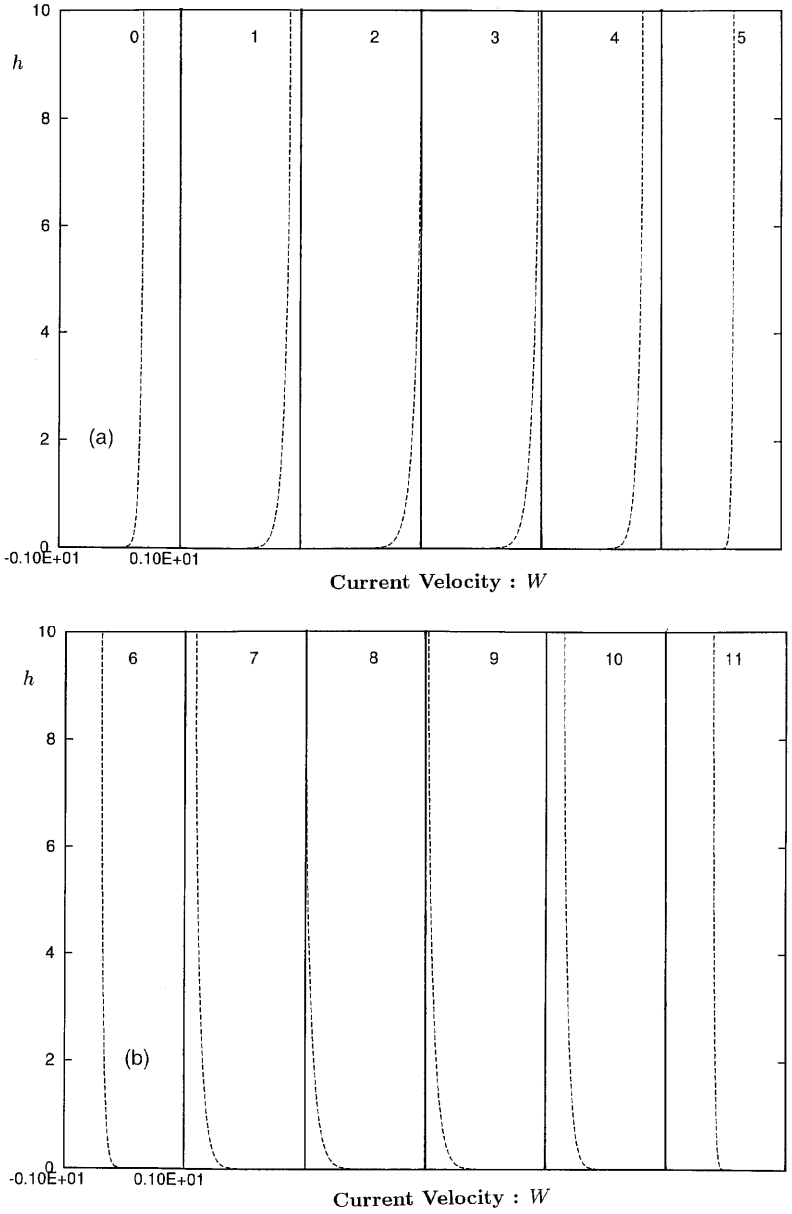

Figure 8. Spanwise current velocity predictions W along height of simulated open sea region across flow cycle $0 \leqslant t \leqslant 11$ h: ---, DSM-IP

Reynolds shear stress profiles plotted against depth are shown in Figures 9(a) and 9(b). The figures follow the qualitative trends reproduced in the rectilinear simulations, namely (a) the strong build-up of turbulence in the near-bed region and (b) its migration towards the free surface, resulting in a linear distribution along the depth of the estuary.

Like the Reynolds shear stress profiles, the highest levels of $\overline{uw}$ are seen in the vicinity of the bed. The DSM-IP predictions suggest that the maximum value of $\overline{uw}$ near the bed is several times larger

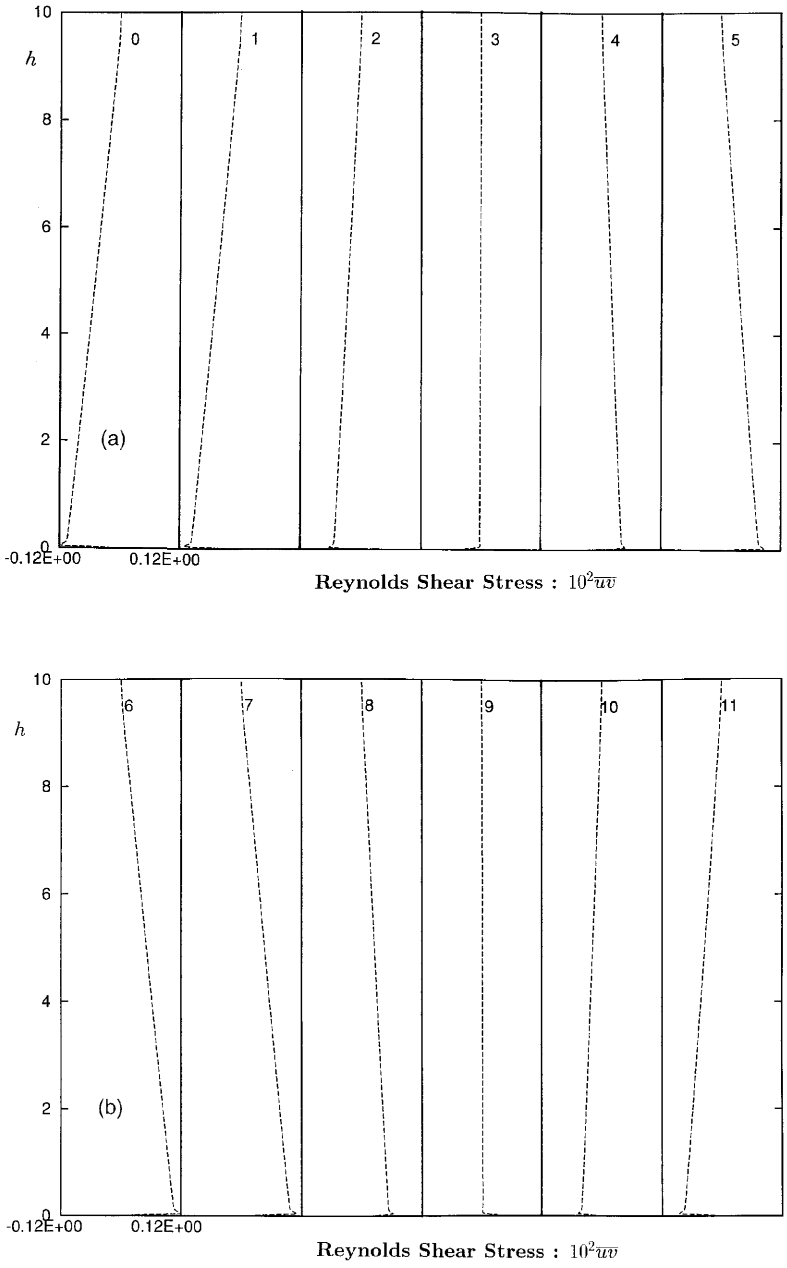

Figure 9. Reynolds shear stress predictions for $\overline{uv}$ along height of simulated open sea region across flow cycle $0 \leqslant t \leqslant 11$ h: ---, DSM-IP

than the maximum value of $\overline{uv}$. This may be associated with the fact that $P_{13} = -\overline{uv}\partial U/\partial y - \overline{vw}\partial W/\partial y$ extracts energy from both current velocity fields, while $P_{12} = \overline{v^2}\partial U/\partial y$ has energy inputs from the U-current velocity only. Furthermore, the near-wall levels of $\overline{uw}$ are not suppressed by pressure pulsations reflecting from the estuary bed.

In the case of $\overline{vw}$ the maximum energy levels are found near the bed. Diffusion away from the bed towards the free surface is also captured in accordance with other shear stress predictions. In general the variation in $\overline{vw}$ with depth is generally linear across the flow cycle.

Like the shear stress profiles, the highest levels of turbulent energy occur in the near-bed region. Diffusion moves some energy towards the free surface during both half-cycles, but the energy profiles do not vary linearly along the depth. In the present DSM-IP simulation the maximum value of k generated in the near-wall region across the flow cycle is approximately 25% *less* than the analogous simulation of Davies[4] (which employed the Vager and Kagan[32] mixing length hypothesis). Since significant levels of k are present in the vicinity of the free surface, it is clear that the turbulent boundary is not fully developed along the depth of the estuary.

Predictions for the normal Reynolds stress $\overline{u^2}$, $\overline{v^2}$ and $\overline{w^2}$ reflect the salient trends observed in the turbulent kinetic energy profiles, particularly the strong near-wall build-up of energy and non-linear distribution with depth. We note that the maximum values of $\overline{u^2}$ and $\overline{w^2}$ are almost identical, while $\overline{v^2}$ is much smaller since its near-bed values are suppressed by the action of pressure reflections.

6.3 Harmonic analysis

The above circular tide simulation is identical to a test case cited by Davies[4] and therefore to complete the analysis we will compare the higher harmonics of the tidal flow predicted with the present DSM model, in particular the semidiurnal period denoted by D_2 (period $30^\circ\,\mathrm{h}^{-1}$) and third-harmonic frequency D_6 (period $90^\circ\,\mathrm{h}^{-1}$). These harmonics were generated by a Fourier analysis after the flow had reached the fully periodic state. The results are presented in Table VI.

Table VI compares three turbulence closures employed by Davies[4] (where the mixing length is based on the time-dependent Vager and Kagan[32] proposal) with the present DSM-IP predictions. Model TKE represents the one-equation k–l model with 50 grids in the vertical direction, while modal(hU) and modal(U^2) are spectral models with 10 modes in the vertical direction which have the advantage of being computationally inexpensive compared with traditional eddy viscosity models. Furthermore, Davies' simulations investigate the effect of the specified time-invariant function $L(y)$ which weights the time-varying mixing length through the vertical. From Table VI it is evident that the Vager and Kagan[32] mixing length proposal predicts the free surface currents to be far less than their steady inviscid values $U_\infty = W_\infty = 1{\cdot}0\,\mathrm{m\,s^{-1}}$. On the other hand, the DSM-IP predictions suggest that at the free surface the U-current velocity is slightly smaller than $U_\infty = 1{\cdot}0\,\mathrm{m\,s^{-1}}$, while the W-current velocity slightly exceeds $W_\infty = 1{\cdot}0\,\mathrm{m\,s^{-1}}$. This suggests that compared with the DSM-IP results the TKE model boundary layer is more turbulent as was deduced in Section 6.2, where we recall that the near-bed DSM-IP turbulent kinetic energy results were 25% less than the Davies[4] predictions.

Discrepancies between the Davies[4] and DSM-IP predictions for the phase angle variation along the vertical, g°, are noted though. However, although corresponding values of g° at the different heights do not match, it is interesting to note that through the vertical direction all harmonics vary by similar amounts regardless of the choice of model. Undoubtedly all the differences noted thus far have to be attributed to the increased model sophistication applied in the present work.

To check whether the discrepancies noted above were genuine we calculated the higher harmonics of a simple test case, namely a rectilinear flow driven by a high-frequency wind wave. Once more the effects of rotation were neglected. The flow parameters are listed in Table VII. The D_2 harmonics are presented in Table VIII.

Here the third-harmonic frequency D_6 is not presented since it is vanishingly small along the depth of the estuary. Table VIII validates the present work, since we note that at the free surface the U-current velocity matches its freestream value $U_\infty = 1\,\mathrm{m\,s^{-1}}$ exactly at $g^\circ = 90^\circ$. These observations

Table VI. Vertical variation in tidal currents at periods D_2 and D_6 computed by Davies (TKE, modal(hU) and modal(U^2)) and present DSM-IP model. All velocities are quoted in cm s^{-1}

		Water depth $h = 10$ m (Vager and Kagan[32] mixing length)													
		Davies,[4] $L(y) = 1$						Davies,[4] $L(y)$ parabolic							
Velocity	h (m)	TKE	g°	Modal (hU)	g°	Modal (U^2)	g°	TKE	g°	Modal(hU)	g°	Modal(U^2)	g°	DSM-IP	g°
$U(D_2)$	10·0	68	197	67	198	65	199	77	198	74	199	73	199	87	1
	1·0	48	197	48	197	46	198	49	198	48	198	47	199	67	0
	0·1	25	197	25	197	24	198	25	198	25	199	24	199	47	0
$U(D_6)$	10·0	4	71	4	67	5	59	4	78	4	72	5	63	3	327
	1·0	1	67	2	65	3	56	2	72	2	69	3	60	2	324
	0·1	—	—	—	—	—	—	—	—	1	68	1	59	1	325
$W(D_2)$	10·0	53	130	52	130	52	129	61	130	57	130	58	129	105	71
	1·0	38	130	37	129	37	129	39	130	37	130	38	128	81	70
	0·1	20	130	19	130	19	129	20	130	20	130	20	128	55	70
$W(D_6)$	10·0	3	353	3	344	5	335	4	359	3	338	5	339	4	44
	1·0	2	349	2	342	3	333	2	353	2	346	3	337	3	11
	0·1	1	348	1	342	1	333	—	—	—	—	1	336	1	33

Table VII. Flow parameters of benchmark simulation

U_∞ (m s^{-1})	T (s)	H (m)	Y_0 (m)
1·0	8	10	0·01

Table VIII. Vertical variation in wind wave currents at D_2. All velocities are quoted in m s^{-1}

Velocity	h (m)	DSM-IP	g°
$U(D_2)$	10·0	100	90
	1·0	100	90
	0·1	100	90

are consistent with a freestream boundary condition for the current velocity $U = U_\infty \sin(\omega t)$, which would usually be the appropriate condition for such a flow (as opposed to a zero-flux condition). Finally, 99% of the water column is represented by the inviscid solution, a similar value to that observed in the simulations of Davies and Jones.[1]

7. CONCLUDING REMARKS

In this paper we have examined both rectilinear and circular tidal flows. The numerical integrations were based on a fully collocated finite volume arrangement which was stabilized through apparent viscosities[15] and source term linearization.[16] In the circular tidal flow calculations a numerical procedure was described ensuring that the substantial derivative in the second-moment equations (9) was materially invariant.

Initial calculations were based on two rectilinear flows, a situation which may be observed in a narrow channel or an estuary where the tide is constrained to one direction only. Both the linear eddy viscosity and DSM models were in very good agreement with the experimental data of McClean[7] (Jade estuary) and Schröder[6] (Elbe estuary). The phase lag between the current velocity and turbulent field was resolved satisfactorily by all turbulence models for both test cases. However, the different-size maxima observed in the experimental data for turbulent kinetic energy profiles in the Elbe estuary were not captured. This was a direct consequence of the simulated flow being driven only by the semidiurnal harmonic D_2 of period 30° h^{-1}. Inevitably though, both sets of experimental data were measured far away from the estuary bed and therefore comparisons with numerical results cannot indicate the relative strength of the turbulence models.

Vertical variations in turbulent variables were also investigated through DSM-IP and DSM-CL simulations which employed two variations of the pressure–strain wall reflection term ϕ^{w}_{ij2}. The salient features observed in rectilinear tidal flows included

(i) the extension of the boundary layer right up to the free surface during most of the flow cycle
(ii) near-bed build-up of turbulence during the flow acceleration stage and its slow decay in the flow deceleration stage due to an increasingly adverse pressure gradient
(iii) a linear variation of Reynolds shear stress profiles with depth during the fully developed turbulent flow stages
(iv) the even distribution of turbulence through the water column at the end of the deceleration stage.

The above remarks have also been observed in References 1 and 4. Furthermore, it was noted that turbulent boundary layers generated by tides were quite different from those created by high-frequency wind wave motions.[11,18] Some physical similarities were present, including the strong production of turbulence energy in the near-bed region and similar pressure–strain mechanics, notably higher levels of $\overline{v^2}$ redistributed from the component $\overline{w^2}$ by the Craft and Launder[23] term for ϕ^{w}_{ij2}. However, tidal boundary layers were found to extend right up to the free surface, where significant levels of turbulence energy were observed in the simulations. Furthermore, the diffusion energy away from the bed is much more significant for tidal flows (compare the present calculations with References 1, 11 and 18).

In the second part of the results section, circular tidal flows were simulated which required the solution of the two-equation system (1) and therefore included the effects of rotation through the Coriolis parameter. The calculations were based on a DSM model with the Gibson and Launder[22] wall reflection term. Following Takhar and Thomas,[24] the Reynolds stress equations were first manipulated to ensure that the convection derivative C_{ij} was invariant. The forcing terms $\partial P/\partial x$ and $\partial P/\partial z$ were also assumed to be out of phase by 45°. Mean velocity profiles showed the same trends demonstrated by the rectilinear tidal flows. In particular, the turbulent boundary layers extended right up to the free surface. It was also noted that near-wall turbulent kinetic energy values were reduced by 25% when compared with the earlier work of Davies.[4]

Comparisons were made between the higher-order harmonics generated by the DSM-IP code and the results of Davies.[4] It was evident that at the free surface the DSM-IP mean velocity predictions exceeded the Davies[4] predictions, again confirming greater levels of turbulent energy in the latter boundary layer. Furthermore, although the DSM-IP predictions along the depth of the estuary did not agree with the results of Davies,[4] it was interesting to note that the range of predicted phase angles through the water column was similar for all models at all higher-order tidal harmonics.

Finally, to see if the discrepancies noted in the harmonic analysis were acceptable, a benchmark simulation was conducted based on a rectilinear flow driven by a high-frequency wind wave (of period $T = 8\,\mathrm{s}$). The fundamental harmonic generated was consistent with a boundary condition for U which was based on $U = U_\infty \sin(\omega t)$.

In summary, although the key features of rectilinear tidal flows can be reproduced with relatively simple (eddy viscosity) turbulence closures, high-Reynolds-number DSM models are required in order to obtain a detailed breakdown of the normal Reynolds stresses. Furthermore, in the case of circular tidal flow, since the Coriolis parameter enters the transport equation governing the Reynolds stresses, it will have an effect on determining the correct levels of turbulent stresses. However, it is very difficult to make a definitive conclusion about the point just raised, since as yet no reliable experimental data are available for detailed comparison in order to validate the present results. We also remark that the numerical scheme adopted here provides a robust algorithm for oscillatory flow problems which remain stable when the flow reverses or relaminarizes.

REFERENCES

1. A. M. Davies and J. E. Jones, 'On the numerical solution of the turbulence energy equations for wae and tidal flows', *Int. j. numer. meth. fluids*, **12**, 17 (1991).
2. T. J. Smith, 'On the representation of Reynolds stresses in estuaries and shallow coastal seas', *J. Phys. Oceanogr.*, **12**, 914 (1982).
3. A. N. Aldridge and A. M. Davies, 'A high-resolution three dimensional hydrodynamic tidal model of the eastern Irish Sea', *J. Phys. Oceanogr.*, **23**, 207 (1993).
4. A. M. Davies, 'On using turbulence energy models to develop spectral viscosity models', *Continental Shelf Res.*, **11**, 1313 (1991).
5. H. Baumert and G. Radach, 'Hysteresis of turbulent kinetic energy in nonrotational tidal flows: a model study', *J. Geophys. Res.*, **97**, 3669 (1992).

6. M. Schröder, 'Messung des turbulenten imupls- und salztransports in der miscchungszone der Elbe', *Tech. Rep. GKSS 87/E/16*, GKSS-Forschungszentrum Geesthacht, 1987.
7. S. R. McClean, *Turbulence and Sediment Transport Measurements in a North Sea Tidal inlet (the Jade)*, Springer, New York, 1983, p. 436.
8. S. G. Sajjadi and J. N. Aldridge, 'Prediction of turbulent flow over rough asymmetrical bed forms', *Appl. Math. Model.*, **19**, 139 (1995).
9. B. E. Launder, D. P. Tselepidakis and B. A. Younis, 'A second-moment closure study of rotating channel flow', *J. Fluid Mech.*, **183**, 63 (1987).
10. B. E. Launder, 'Second-moment closure: present . . . and future?', *Int. J. Heat Fluid Flow*, **10**, 282 (1989).
11. S. G. Sajjadi and M. N. Waywell, 'Application of roughness – dependent boundary conditions to turbulent oscillatory flows'. *Int. J. Heat Fluid Flow*, **18**, 368 (1997).
12. H. O. Anwar and R. Atkins, 'Turbulence measurements in simulated tidal flow', *J. Hydraul. Div. ASCE*, **8**, 1273 (1980).
13. C. M. Gordon, 'Sediment entrainment and suspension in a turbulent tidal flow', *Marine Geol.*, **18**, M57 (1975).
14. D. Hamilton, J. H. Sommerville and P. N. Stanford, 'Bottom currents and shelf sediments, southwest of Britain', *Sediment. Geol.*, **26**, 115 (1980).
15. F. S. Lien and M. A. Leschziner, 'A general non-orthogonal collocated *FV* algorithm for turbulent flow at all speeds incorporating second-moment closure', *Tech. Rep. TFD/92/4*, Department of Mechanical Engineering, UMIST, 1992.
16. S. V. Patankar, *Numerical Heat Transfer and Fluid Flow*, McGraw-Hill, New York, 1980.
17. J. N. Aldridge, 'A continuum mixture theory to sediment transport with application to turbulent oscillatory boundary layers', *Ph.D. Thesis*, University of Plymouth, 1989.
18. M. N. Waywell and S. G. Sajjadi, 'Transition from laminar to turbulence in oscillatory boundary layer flows over a smooth flat plate. *J. Math. Engng. Ind.*, **6**, 79 (1997).
19. M. N. Waywell, 'Predictions of wave and tidally induced oscillatory flows with Reynolds stress turbulence models', *Ph.D. Thesis*, University of Salford, 1995.
20. B. E. Launder, G. J. Reece and W. Rodi, 'Asymptotic near-wall stress dissipation rates in a turbulent flow'. *J. Fluid Mech.*, **68**, 537 (1975).
21. C. C. Shir, 'A preliminary study of atmospheric turbulent flow in the idealized planetary boundary layer', *J. Atmos. Sci.*, **30**, 1327 (1973).
22. M. M. Gibson and B. E. Launder, 'Ground effects on pressure fluctuations in the atmospheric boundary layer', *J. Fluid Mech.*, **86**, 491 (1978).
23. T. J. Craft and B. E. Launder, 'New wall-reflection model applied to the turbulent impinging jet', *AIAA J.*, **30**, 2970 (1992).
24. H. S. Takhar and T. G. Thomas, 'Frame invariance of turbulence constitutive equations', *Tech. Rep.*, Simon Engineering Laboratories, University of Manchester, 1985.
25. H. Schlichting, *Boundary-Layer Theory*, 6th edn, McGraw-Hill, New York, 1968.
26. B. G. Krishnappen, 'Laboratory verification of a turbulent flow model', *J. Hydraul. Engng. ASCE*, **110**, 500 (1984).
27. J. Nikuradse, 'Stromungsgesetze in rauhen Rohren', *Forschg. Geb. Ing.-Wesens*, **361**, (1933).
28. W. Rodi, 'Turbulenzmodelle und ihre Anwendungen auf Probleme des Wasseerbaus', *Dr. Habil. Thesis 138*, University of Karlsruhe, 1978.
29. M. S. Hossain, 'Mathematische Modellierung von turbulente Auftriebströmungen', *Dr. Habil. Thesis 145*, University of Karlsruhe, 1980.
30. M. Hino, M. Kashiwayanag, A. Nakayama and T. Hara, 'Experiments on the turbulence statistics and the structure of a reciprocating oscillatory flow', *J. Fluid Mech.*, **131**, 263 (1983).
31. B. L. Jensen, B. M. Sumer and J. Fredsøe, 'Turbulent oscillatory boundary layers at high Reynolds numbers', *J. Fluid Mech.*, **206**, 265 (1989).
32. B. G. Vager and B. A. Kagan, 'The dynamics of the turbulent boundary layer in a tidal current', *Atmos. Oceanic Phys.*, **5**, 168 (1969).